2009

Measurement of the top quark mass in final states with two leptons

V. M. Abazov
Joint Institute for Nuclear Research, Dubna, Russia

Kenneth A. Bloom
University of Nebraska-Lincoln, kenbloom@unl.edu

Gregory R. Snow
University of Nebraska-Lincoln, gsnow1@unl.edu

D0 Collaboration

Measurement of the top quark mass in final states with two leptons

V. M. Abazov,[37] B. Abbott,[75] M. Abolins,[65] B. S. Acharya,[30] M. Adams,[51] T. Adams,[49] E. Aguilo,[6] M. Ahsan,[59] G. D. Alexeev,[37] G. Alkhazov,[41] A. Alton,[64] G. Alverson,[63] G. A. Alves,[2] L. S. Ancu,[36] T. Andeen,[53] M. S. Anzelc,[53] M. Aoki,[50] Y. Arnoud,[14] M. Arov,[60] M. Arthaud,[18] A. Askew,[49] B. Åsman,[42] O. Atramentov,[49] C. Avila,[8] J. BackusMayes,[82] F. Badaud,[13] L. Bagby,[50] B. Baldin,[50] D. V. Bandurin,[59] S. Banerjee,[30] E. Barberis,[63] A.-F. Barfuss,[15] P. Bargassa,[80] P. Baringer,[58] J. Barreto,[2] J. F. Bartlett,[50] U. Bassler,[18] D. Bauer,[44] S. Beale,[6] A. Bean,[58] M. Begalli,[3] M. Begel,[73] C. Belanger-Champagne,[42] L. Bellantoni,[50] A. Bellavance,[50] J. A. Benitez,[65] S. B. Beri,[28] G. Bernardi,[17] R. Bernhard,[23] I. Bertram,[43] M. Besançon,[18] R. Beuselinck,[44] V. A. Bezzubov,[40] P. C. Bhat,[50] V. Bhatnagar,[28] G. Blazey,[52] S. Blessing,[49] K. Bloom,[67] A. Boehnlein,[50] D. Boline,[62] T. A. Bolton,[59] E. E. Boos,[39] G. Borissov,[43] T. Bose,[62] A. Brandt,[78] O. Brandt,[22] R. Brock,[65] G. Brooijmans,[70] A. Bross,[50] D. Brown,[19] X. B. Bu,[7] D. Buchholz,[53] M. Buehler,[81] V. Buescher,[22] V. Bunichev,[39] S. Burdin,[43] T. H. Burnett,[82] C. P. Buszello,[44] P. Calfayan,[26] B. Calpas,[15] S. Calvet,[16] J. Cammin,[71] M. A. Carrasco-Lizarraga,[34] E. Carrera,[49] W. Carvalho,[3] B. C. K. Casey,[50] H. Castilla-Valdez,[34] S. Chakrabarti,[72] D. Chakraborty,[52] K. M. Chan,[55] A. Chandra,[48] E. Cheu,[46] D. K. Cho,[62] S. Choi,[33] B. Choudhary,[29] T. Christoudias,[44] S. Cihangir,[50] D. Claes,[67] J. Clutter,[58] M. Cooke,[50] W. E. Cooper,[50] M. Corcoran,[80] F. Couderc,[18] M.-C. Cousinou,[15] S. Crépé-Renaudin,[14] V. Cuplov,[59] D. Cutts,[77] M. Ćwiok,[31] A. Das,[46] G. Davies,[44] K. De,[78] S. J. de Jong,[36] E. De La Cruz-Burelo,[34] K. DeVaughan,[67] F. Déliot,[18] M. Demarteau,[50] R. Demina,[71] D. Denisov,[50] S. P. Denisov,[40] S. Desai,[50] H. T. Diehl,[50] M. Diesburg,[50] A. Dominguez,[67] T. Dorland,[82] A. Dubey,[29] L. V. Dudko,[39] L. Duflot,[16] D. Duggan,[49] A. Duperrin,[15] S. Dutt,[28] A. Dyshkant,[52] M. Eads,[67] D. Edmunds,[65] J. Ellison,[48] V. D. Elvira,[50] Y. Enari,[77] S. Eno,[61] P. Ermolov,[39] M. Escalier,[15] H. Evans,[54] A. Evdokimov,[73] V. N. Evdokimov,[40] G. Facini,[63] A. V. Ferapontov,[59] T. Ferbel,[61] F. Fiedler,[25] F. Filthaut,[36] W. Fisher,[50] H. E. Fisk,[50] M. Fortner,[52] H. Fox,[43] S. Fu,[50] S. Fuess,[50] T. Gadfort,[70] C. F. Galea,[36] A. Garcia-Bellido,[71] V. Gavrilov,[38] P. Gay,[13] W. Geist,[19] W. Geng,[15] C. E. Gerber,[51] Y. Gershtein,[49] D. Gillberg,[6] G. Ginther,[50] B. Gómez,[8] A. Goussiou,[82] P. D. Grannis,[72] S. Greder,[19] H. Greenlee,[50] Z. D. Greenwood,[60] E. M. Gregores,[4] G. Grenier,[20] Ph. Gris,[13] J.-F. Grivaz,[16] A. Grohsjean,[26] S. Grünendahl,[50] M. W. Grünewald,[31] F. Guo,[72] J. Guo,[72] G. Gutierrez,[50] P. Gutierrez,[75] A. Haas,[70] N. J. Hadley,[61] P. Haefner,[26] S. Hagopian,[49] J. Haley,[68] I. Hall,[65] R. E. Hall,[47] L. Han,[7] K. Harder,[45] A. Harel,[71] J. M. Hauptman,[57] J. Hays,[44] T. Hebbeker,[21] D. Hedin,[52] J. G. Hegeman,[35] A. P. Heinson,[48] U. Heintz,[62] C. Hensel,[24] I. Heredia-De La Cruz,[34] K. Herner,[64] G. Hesketh,[63] M. D. Hildreth,[55] R. Hirosky,[81] T. Hoang,[49] J. D. Hobbs,[72] B. Hoeneisen,[12] M. Hohlfeld,[22] S. Hossain,[75] P. Houben,[35] Y. Hu,[72] Z. Hubacek,[10] N. Huske,[17] V. Hynek,[10] I. Iashvili,[69] R. Illingworth,[50] A. S. Ito,[50] S. Jabeen,[62] M. Jaffré,[16] S. Jain,[75] K. Jakobs,[23] D. Jamin,[15] C. Jarvis,[61] R. Jesik,[44] K. Johns,[46] C. Johnson,[70] M. Johnson,[50] D. Johnston,[67] A. Jonckheere,[50] P. Jonsson,[44] A. Juste,[50] E. Kajfasz,[15] D. Karmanov,[39] P. A. Kasper,[50] I. Katsanos,[67] V. Kaushik,[78] R. Kehoe,[79] S. Kermiche,[15] N. Khalatyan,[50] A. Khanov,[76] A. Kharchilava,[69] Y. N. Kharzheev,[37] D. Khatidze,[70] T. J. Kim,[32] M. H. Kirby,[53] M. Kirsch,[21] B. Klima,[50] J. M. Kohli,[28] J.-P. Konrath,[23] A. V. Kozelov,[40] J. Kraus,[65] T. Kuhl,[25] A. Kumar,[69] A. Kupco,[11] T. Kurča,[20] V. A. Kuzmin,[39] J. Kvita,[9] F. Lacroix,[13] D. Lam,[55] S. Lammers,[54] G. Landsberg,[77] P. Lebrun,[20] W. M. Lee,[50] A. Leflat,[39] J. Lellouch,[17] J. Li,[78] L. Li,[48] Q. Z. Li,[50] S. M. Lietti,[5] J. K. Lim,[32] D. Lincoln,[50] J. Linnemann,[65] V. V. Lipaev,[40] R. Lipton,[50] Y. Liu,[7] Z. Liu,[6] A. Lobodenko,[41] M. Lokajicek,[11] P. Love,[43] H. J. Lubatti,[82] R. Luna-Garcia,[34] A. L. Lyon,[50] A. K. A. Maciel,[2] D. Mackin,[80] P. Mättig,[27] A. Magerkurth,[64] P. K. Mal,[82] H. B. Malbouisson,[3] S. Malik,[67] V. L. Malyshev,[37] Y. Maravin,[59] B. Martin,[14] R. McCarthy,[72] C. L. McGivern,[58] M. M. Meijer,[36] A. Melnitchouk,[66] L. Mendoza,[8] D. Menezes,[52] P. G. Mercadante,[5] M. Merkin,[39] K. W. Merritt,[50] A. Meyer,[21] J. Meyer,[24] J. Mitrevski,[70] R. K. Mommsen,[45] N. K. Mondal,[30] R. W. Moore,[6] T. Moulik,[58] G. S. Muanza,[15] M. Mulhearn,[70] O. Mundal,[22] L. Mundim,[3] E. Nagy,[15] M. Naimuddin,[50] M. Narain,[77] H. A. Neal,[64] J. P. Negret,[8] P. Neustroev,[41] H. Nilsen,[23] H. Nogima,[3] S. F. Novaes,[5] T. Nunnemann,[26] G. Obrant,[41] C. Ochando,[16] D. Onoprienko,[59] J. Orduna,[34] N. Oshima,[50] N. Osman,[44] J. Osta,[55] R. Otec,[10] G. J. Otero y Garzón,[1] M. Owen,[45] M. Padilla,[48] P. Padley,[80] M. Pangilinan,[77] N. Parashar,[56] S.-J. Park,[24] S. K. Park,[32] J. Parsons,[70] R. Partridge,[77] N. Parua,[54] A. Patwa,[73] G. Pawloski,[80] B. Penning,[23] M. Perfilov,[39] K. Peters,[45] Y. Peters,[45] P. Pétroff,[16] R. Piegaia,[1] J. Piper,[65] M.-A. Pleier,[22] P. L. M. Podesta-Lerma,[34] V. M. Podstavkov,[50] Y. Pogorelov,[55] M.-E. Pol,[2] P. Polozov,[38] A. V. Popov,[40] C. Potter,[6] W. L. Prado da Silva,[3] S. Protopopescu,[73] J. Qian,[64] A. Quadt,[24] B. Quinn,[66] A. Rakitine,[43] M. S. Rangel,[16] K. Ranjan,[29] P. N. Ratoff,[43] P. Renkel,[79] P. Rich,[45] M. Rijssenbeek,[72] I. Ripp-Baudot,[19] F. Rizatdinova,[76] S. Robinson,[44] R. F. Rodrigues,[3] M. Rominsky,[75] C. Royon,[18] P. Rubinov,[50] R. Ruchti,[55] G. Safronov,[38] G. Sajot,[14] A. Sánchez-Hernández,[34] M. P. Sanders,[17] B. Sanghi,[50] G. Savage,[50] L. Sawyer,[60] T. Scanlon,[44] D. Schaile,[26] R. D. Schamberger,[72] Y. Scheglov,[41] H. Schellman,[53] T. Schliephake,[27] S. Schlobohm,[82] C. Schwanenberger,[45] R. Schwienhorst,[65] J. Sekaric,[49] H. Severini,[75]

E. Shabalina,[24] M. Shamim,[59] V. Shary,[18] A. A. Shchukin,[40] R. K. Shivpuri,[29] V. Siccardi,[19] V. Simak,[10] V. Sirotenko,[50] P. Skubic,[75] P. Slattery,[71] D. Smirnov,[55] G. R. Snow,[67] J. Snow,[74] S. Snyder,[73] S. Söldner-Rembold,[45] L. Sonnenschein,[21] A. Sopczak,[43] M. Sosebee,[78] K. Soustruznik,[9] B. Spurlock,[78] J. Stark,[14] V. Stolin,[38] D. A. Stoyanova,[40] J. Strandberg,[64] S. Strandberg,[42] M. A. Strang,[69] E. Strauss,[72] M. Strauss,[75] R. Ströhmer,[26] D. Strom,[53] L. Stutte,[50] S. Sumowidagdo,[49] P. Svoisky,[36] M. Takahashi,[45] A. Tanasijczuk,[1] W. Taylor,[6] B. Tiller,[26] F. Tissandier,[13] M. Titov,[18] V. V. Tokmenin,[37] I. Torchiani,[23] D. Tsybychev,[72] B. Tuchming,[18] C. Tully,[68] P. M. Tuts,[70] R. Unalan,[65] L. Uvarov,[41] S. Uvarov,[41] S. Uzunyan,[52] B. Vachon,[6] P. J. van den Berg,[35] R. Van Kooten,[54] W. M. van Leeuwen,[35] N. Varelas,[51] E. W. Varnes,[46] I. A. Vasilyev,[40] P. Verdier,[20] L. S. Vertogradov,[37] M. Verzocchi,[50] D. Vilanova,[18] P. Vint,[44] P. Vokac,[10] M. Voutilainen,[67] R. Wagner,[68] H. D. Wahl,[49] M. H. L. S. Wang,[71] J. Warchol,[55] G. Watts,[82] M. Wayne,[55] G. Weber,[25] M. Weber,[50] L. Welty-Rieger,[54] A. Wenger,[23] M. Wetstein,[61] A. White,[78] D. Wicke,[25] M. R. J. Williams,[43] G. W. Wilson,[58] S. J. Wimpenny,[48] M. Wobisch,[60] D. R. Wood,[63] T. R. Wyatt,[45] Y. Xie,[77] C. Xu,[64] S. Yacoob,[53] R. Yamada,[50] W.-C. Yang,[45] T. Yasuda,[50] Y. A. Yatsunenko,[37] Z. Ye,[50] H. Yin,[7] K. Yip,[73] H. D. Yoo,[77] S. W. Youn,[53] J. Yu,[78] C. Zeitnitz,[27] S. Zelitch,[81] T. Zhao,[82] B. Zhou,[64] J. Zhu,[72] M. Zielinski,[71] D. Zieminska,[54] L. Zivkovic,[70] V. Zutshi,[52] and E. G. Zverev[39]

(The D0 Collaboration)*

[1]*Universidad de Buenos Aires, Buenos Aires, Argentina*
[2]*LAFEX, Centro Brasileiro de Pesquisas Físicas, Rio de Janeiro, Brazil*
[3]*Universidade do Estado do Rio de Janeiro, Rio de Janeiro, Brazil*
[4]*Universidade Federal do ABC, Santo André, Brazil*
[5]*Instituto de Física Teórica, Universidade Estadual Paulista, São Paulo, Brazil*
[6]*University of Alberta, Edmonton, Alberta, Canada; Simon Fraser University, Burnaby, British Columbia, Canada; York University, Toronto, Ontario, Canada and McGill University, Montreal, Quebec, Canada*
[7]*University of Science and Technology of China, Hefei, People's Republic of China*
[8]*Universidad de los Andes, Bogotá, Colombia*
[9]*Center for Particle Physics, Charles University, Faculty of Mathematics and Physics, Prague, Czech Republic*
[10]*Czech Technical University in Prague, Prague, Czech Republic*
[11]*Center for Particle Physics, Institute of Physics, Academy of Sciences of the Czech Republic, Prague, Czech Republic*
[12]*Universidad San Francisco de Quito, Quito, Ecuador*
[13]*LPC, Université Blaise Pascal, CNRS/IN2P3, Clermont, France*
[14]*LPSC, Université Joseph Fourier Grenoble 1, CNRS/IN2P3, Institut National Polytechnique de Grenoble, Grenoble, France*
[15]*CPPM, Aix-Marseille Université, CNRS/IN2P3, Marseille, France*
[16]*LAL, Université Paris-Sud, IN2P3/CNRS, Orsay, France*
[17]*LPNHE, IN2P3/CNRS, Universités Paris VI and VII, Paris, France*
[18]*CEA, Irfu, SPP, Saclay, France*
[19]*IPHC, Université de Strasbourg, CNRS/IN2P3, Strasbourg, France*
[20]*IPNL, Université Lyon 1, CNRS/IN2P3, Villeurbanne, France and Université de Lyon, Lyon, France*
[21]*III. Physikalisches Institut A, RWTH Aachen University, Aachen, Germany*
[22]*Physikalisches Institut, Universität Bonn, Bonn, Germany*
[23]*Physikalisches Institut, Universität Freiburg, Freiburg, Germany*
[24]*II. Physikalisches Institut, Georg-August-Universität G Göttingen, Germany*
[25]*Institut für Physik, Universität Mainz, Mainz, Germany*
[26]*Ludwig-Maximilians-Universität München, München, Germany*
[27]*Fachbereich Physik, University of Wuppertal, Wuppertal, Germany*
[28]*Panjab University, Chandigarh, India*
[29]*Delhi University, Delhi, India*
[30]*Tata Institute of Fundamental Research, Mumbai, India*
[31]*University College Dublin, Dublin, Ireland*
[32]*Korea Detector Laboratory, Korea University, Seoul, Korea*
[33]*SungKyunKwan University, Suwon, Korea*
[34]*CINVESTAV, Mexico City, Mexico*
[35]*FOM-Institute NIKHEF and University of Amsterdam/NIKHEF, Amsterdam, The Netherlands*
[36]*Radboud University Nijmegen/NIKHEF, Nijmegen, The Netherlands*
[37]*Joint Institute for Nuclear Research, Dubna, Russia*
[38]*Institute for Theoretical and Experimental Physics, Moscow, Russia*
[39]*Moscow State University, Moscow, Russia*
[40]*Institute for High Energy Physics, Protvino, Russia*
[41]*Petersburg Nuclear Physics Institute, St. Petersburg, Russia*

[42]Stockholm University, Stockholm, Sweden, and Uppsala University, Uppsala, Sweden
[43]Lancaster University, Lancaster, United Kingdom
[44]Imperial College, London, United Kingdom
[45]University of Manchester, Manchester, United Kingdom
[46]University of Arizona, Tucson, Arizona 85721, USA
[47]California State University, Fresno, California 93740, USA
[48]University of California, Riverside, California 92521, USA
[49]Florida State University, Tallahassee, Florida 32306, USA
[50]Fermi National Accelerator Laboratory, Batavia, Illinois 60510, USA
[51]University of Illinois at Chicago, Chicago, Illinois 60607, USA
[52]Northern Illinois University, DeKalb, Illinois 60115, USA
[53]Northwestern University, Evanston, Illinois 60208, USA
[54]Indiana University, Bloomington, Indiana 47405, USA
[55]University of Notre Dame, Notre Dame, Indiana 46556, USA
[56]Purdue University Calumet, Hammond, Indiana 46323, USA
[57]Iowa State University, Ames, Iowa 50011, USA
[58]University of Kansas, Lawrence, Kansas 66045, USA
[59]Kansas State University, Manhattan, Kansas 66506, USA
[60]Louisiana Tech University, Ruston, Louisiana 71272, USA
[61]University of Maryland, College Park, Maryland 20742, USA
[62]Boston University, Boston, Massachusetts 02215, USA
[63]Northeastern University, Boston, Massachusetts 02115, USA
[64]University of Michigan, Ann Arbor, Michigan 48109, USA
[65]Michigan State University, East Lansing, Michigan 48824, USA
[66]University of Mississippi, University, Mississippi 38677, USA
[67]University of Nebraska, Lincoln, Nebraska 68588, USA
[68]Princeton University, Princeton, New Jersey 08544, USA
[69]State University of New York, Buffalo, New York 14260, USA
[70]Columbia University, New York, New York 10027, USA
[71]University of Rochester, Rochester, New York 14627, USA
[72]State University of New York, Stony Brook, New York 11794, USA
[73]Brookhaven National Laboratory, Upton, New York 11973, USA
[74]Langston University, Langston, Oklahoma 73050, USA
[75]University of Oklahoma, Norman, Oklahoma 73019, USA
[76]Oklahoma State University, Stillwater, Oklahoma 74078, USA
[77]Brown University, Providence, Rhode Island 02912, USA
[78]University of Texas, Arlington, Texas 76019, USA
[79]Southern Methodist University, Dallas, Texas 75275, USA
[80]Rice University, Houston, Texas 77005, USA
[81]University of Virginia, Charlottesville, Virginia 22901, USA
[82]University of Washington, Seattle, Washington 98195, USA

(Received 22 April 2009; published 20 November 2009)

We present measurements of the top quark mass (m_t) in $t\bar{t}$ candidate events with two final state leptons using 1 fb^{-1} of data collected by the D0 experiment. Our data sample is selected by requiring two fully identified leptons or by relaxing one lepton requirement to an isolated track if at least one jet is tagged as a b jet. The top quark mass is extracted after reconstructing the event kinematics under the $t\bar{t}$ hypothesis using two methods. In the first method, we integrate over expected neutrino rapidity distributions, and in the second we calculate a weight for the possible top quark masses based on the observed particle momenta and the known parton distribution functions. We analyze 83 candidate events in the data and obtain $m_t = 176.2 \pm 4.8(\text{stat}) \pm 2.1(\text{sys})$ GeV and $m_t = 173.2 \pm 4.9(\text{stat}) \pm 2.0(\text{sys})$ GeV for the two methods, respectively. Accounting for correlations between the two methods, we combine the measurements to obtain $m_t = 174.7 \pm 4.4(\text{stat}) \pm 2.0(\text{sys})$ GeV.

DOI: 10.1103/PhysRevD.80.092006 PACS numbers: 12.15.Ff, 14.65.Ha

I. INTRODUCTION

After the top quark was discovered in 1995 [1,2], emphasis quickly turned to detailed studies of its properties

*http://www-d0.fnal.gov

including measuring its mass across all reconstructable final states. Within the standard model, a precise measurement of the top quark mass (m_t) and W boson mass (M_W) can be used to constrain the Higgs boson mass (M_{H}). In fact, these masses can be related by radiative corrections to M_W. One-loop corrections give $M_W^2 = \frac{\pi\alpha/\sqrt{2}G_F}{\sin^2\theta_W(1-\Delta r)}$, where Δr depends quadratically on m_t and logarithmically on M_{H} [3]. Beyond its relation to M_{H}, the top quark mass reflects the Yukawa coupling, Y_t, for the top quark via $Y_t = m_t\sqrt{2}/v$, where $v = 246$ GeV is the vacuum expectation value of the Higgs field [4]. Given that these couplings are not predicted by the theory, $Y_t = 0.995 \pm 0.007$ for the current m_t [5] is curiously close to unity. One of several possible modifications to the mechanism underlying electroweak symmetry breaking suggests a more central role for the top quark. For instance, in top-color assisted technicolor [6,7], the top quark plays a major role in electroweak symmetry breaking. These models entirely remove the need for an elementary scalar Higgs field in favor of new strong interactions that provide the observed mass spectrum. Perhaps there are extra Higgs doublets as in MSSM models [8]; measurement of the top quark mass may be sensitive to such models (e.g., Ref. [9]).

In the standard model, $\mathrm{BR}(t \to Wb)$ is expected to be nearly 100%. So the relative rates of final states in events with top quark pairs, $t\bar{t}$, are dictated by the branching ratios of the W boson to various fermion pairs. In approximately 10% of $t\bar{t}$ events, both W bosons decay leptonically. Generally, only events that include the $W \to e\nu$ and $W \to \mu\nu$ modes yield final states with precisely reconstructed lepton momenta that can be used for mass analysis. Thus, analyzable dilepton final states are $t\bar{t} \to \ell\bar{\ell}' + \bar{\nu}\nu' + b\bar{b}$, where $\ell, \ell' = e, \mu$. We measure m_t in these dilepton events. The $W \to \tau\nu \to e(\mu)\nu\bar{\nu}$ decay modes cannot be separated from the direct $W \to e(\mu)\nu$ decays and are included in our analysis.

Dilepton channels provide a sample that is statistically independent of the more copious $t\bar{t} \to \ell\nu + q\bar{q}' + b\bar{b}$ (ℓ + jets) decays. The relative contributions of specific systematic effects are somewhat different between mass measurements from events with dilepton or ℓ + jets final states. The jet multiplicity and the dominant background processes are different. The measurement of m_t in the dilepton channel also provides a consistency test of the $t\bar{t}$ event sample with the expected $t \to Wb$ decay. Nonstandard decays of the top quark, such as $t \to H^{\pm}b$, can affect the final state particle kinematics differently in different $t\bar{t}$ channels. These kinematics affect the reconstructed mass significantly, for example, in the ℓ + jets channel [10]. Therefore, it is important to precisely test the consistency of the m_t measurements in different channels.

Previous efforts to measure m_t in the dilepton channels have been pursued by the D0 and CDF Collaborations. A frequently used technique reconstructs individual event kinematics using known constraints to obtain a relative probability of consistency with a range of top quark masses. The "matrix weighting" method (MWT) follows the ideas proposed by Dalitz and Goldstein [11] and Kondo [12]. It uses partial production and decay information by employing parton distribution functions and observed particle momenta to obtain a mass estimate for each dilepton event, and has previously been implemented by D0 [13,14]. The "neutrino weighting" method (νWT) was developed at D0 [13]. It integrates over expected neutrino rapidity distributions, and has been used by both the D0 [13,14] and CDF [15] Collaborations.

In this paper, we describe a measurement of the top quark mass in 1 fb^{-1} of $p\bar{p}$ collider data collected using the D0 detector at the Fermilab Tevatron Collider. Events are selected in two categories. Those with one fully identified electron and one fully identified muon, two electrons, or two muons are referred to as "2ℓ." To improve acceptance, we include a second category consisting of events with only one fully reconstructed electron or muon and an isolated high transverse momentum (p_T) track as well as at least one identified b jet, which we refer to as "ℓ + track" events. We describe the detection, selection, and modeling of these events in Secs. II and III. Reconstruction of the kinematics of $t\bar{t}$ events proceeds by both the MWT and νWT approaches. These methods are described in Sec. IV. In Sec. V, we describe the maximum likelihood fits to extract m_t from data. Finally, we discuss our results and systematic uncertainties in Sec. VI.

II. DETECTOR AND DATA SAMPLE

A. Detector components

The D0 Run II detector [16] is a multipurpose collider detector consisting of an inner magnetic central tracking system, calorimeters, and outer muon tracking detectors. The spatial coordinates of the D0 detector are defined as follows: the positive z axis is along the direction of the proton beam while positive y is defined as upward from the detector's center, which serves as the origin. The polar angle θ is measured with respect to the positive z direction and is usually expressed as the pseudorapidity, $\eta \equiv -\ln[\tan(\theta/2)]$. The azimuthal angle ϕ is measured with respect to the positive x direction, which points away from the center of the Tevatron ring.

The inner tracking detectors are responsible for measuring the trajectories and momenta of charged particles and for locating track vertices. They reside inside a superconducting solenoid that generates a magnetic field of 2 T. A silicon microstrip tracker (SMT) is innermost and provides precision position measurements, particularly in the azimuthal plane, which allow the reconstruction of displaced secondary vertices from the decay of long-lived particles. This permits identification of jets from heavy flavor quarks, particularly b quarks. A central fiber tracker is composed of scintillating fibers mounted on eight concentric support cylinders. Each cylinder supports one axial and one stereo

layer of fibers, alternating by $\pm 3^\circ$ relative to the cylinder axis. The outermost cylinder provides coverage for $|\eta| < 1.7$. The position resolution in the transverse plane of the event primary vertex is measured to be $\sigma(r\phi) = 35\ \mu$m. In the region $|\eta| < 1.62$, the momentum resolution for the combined tracking is given by the expression $\sigma(1/p_T)/(1/p_T) = 0.003 p_T \oplus 0.026/\sqrt{\sin\theta}$.

The calorimeter measures electron and jet energies, directions, and shower shapes relevant for particle identification. Neutrinos are also measured via the calorimeters' hermeticity and the constraint of momentum conservation in the plane transverse to the beam direction. Three liquid argon filled cryostats containing primarily uranium absorbers constitute the central and end cap calorimeter systems. The former covers $|\eta| < 1.1$, and the latter extends coverage to $|\eta| = 4.2$. Each calorimeter consists of an electromagnetic (EM) section followed longitudinally by hadronic sections. Readout cells are arranged in a pseudoprojective geometry with respect to the nominal interaction region. Electron energy resolution in the central calorimeter away from the intercryostat crack is measured to be $\sigma(E)/E = 0.47/E \oplus 0.24/\sqrt{E} \oplus 0.03$. Jets are measured to have a resolution of $\sigma(p_T)/p_T = 2.07/p_T \oplus 0.703/\sqrt{p_T} \oplus 0.0577$ in the region $|\eta| < 0.4$.

Drift tubes and scintillators are arranged in planes outside the calorimeter system to identify and measure the trajectories of penetrating muons. One drift tube layer resides inside iron toroids with a magnetic field of 1.8 T, while two more layers are located outside. The coverage of the muon system is $|\eta| < 2$.

B. Data sample

The D0 trigger and data acquisition systems are designed to accommodate instantaneous luminosities up to $3 \times 10^{32}\ \text{cm}^{-2}\,\text{s}^{-1}$. The Tevatron operates with 396 ns spacing between proton (antiproton) bunches and delivers a 2 MHz bunch crossing rate. For our data sample, each crossing yields on average 1.2 $p\bar{p}$ interactions.

Luminosity measurement at D0 is based on the rate of inelastic $p\bar{p}$ collisions observed by plastic scintillation counters mounted on the inner faces of the calorimeter end cap cryostats. Based on information from the tracking, calorimeter, and muon systems, the first level of the trigger limits the rate for accepted events to 2 kHz. This is a dedicated hardware trigger. Second and third level triggers employ algorithms running in processors to reduce the output rate to about 100 Hz, which is written to tape.

Several different triggers are used for the five decay channels considered in this measurement. We employ single electron triggers for the ee and e + track channels and single muon triggers for the $\mu\mu$ and μ + track channels. The $e\mu$ analysis employs all unprescaled triggers requiring one electron and/or one muon. We also use triggers requiring one lepton plus one jet for the ℓ + track channels. A slight difference between the νWT and MWT analyses occurs because the latter excludes 2% of the data collected while the single muon trigger was prescaled. While the effect on the kinematic distributions is negligible, this results in one less $\mu\mu$ candidate event in the final sample for the MWT analysis.

Events were collected with these triggers at D0 between April 2002 and February 2006 with $\sqrt{s} = 1.96$ TeV. Data quality requirements remove events for which the tracker, calorimeter, or muon system are known to be functioning improperly. The integrated luminosity of the analyzed data sample is about 1 fb^{-1}.

C. Particle identification

We reconstruct the recorded data to identify and measure final state particles, as described below. The primary event vertex (PV) is identified as the vertex with the lowest probability to come from a soft $p\bar{p}$ interaction based on the transverse momenta of associated tracks. We select events in which the PV is reconstructed from at least three tracks and with $|z_{PV}| < 60$ cm. Secondary vertices from the decay of long-lived particles from the hard interaction are reconstructed from two or more tracks satisfying the requirements of $p_T > 1$ GeV and more than one hit in the SMT. We require each track to have a large impact parameter significance, $\text{DCA}/\sigma_{\text{DCA}} > 3.5$, with respect to the PV, where DCA is the distance of the track's closest approach to the PV in the transverse plane.

High-p_T muons are identified by matching tracks in the inner tracker with those in the muon system. The track requirements include a cut on $\text{DCA} < 0.02\,(0.2)$ cm for tracks with (without) SMT hits. Muons are isolated in the tracker when the sum of track momenta in a cone of radius $\Delta\mathcal{R}(\text{muon, track}) = \sqrt{(\Delta\eta)^2 + (\Delta\phi)^2} = 0.5$ around the muon's matching track is small compared to the track p_T. We also require isolated muons to have the sum of calorimeter cell energies in an annulus with radius in the range $0.1 < \Delta\mathcal{R} < 0.4$ around the matched track to be low compared to the matching track p_T.

High-p_T isolated tracks are identified solely in the inner tracker. We require them to satisfy track isolation requirements and to be separated from calorimeter jets by $\Delta\mathcal{R}(\text{jet, track}) > 0.5$. These tracks must correspond to leptons from the PV, so we also require that $\text{DCA}/\sigma_{\text{DCA}} < 2.5$. We avoid double-counting leptons by requiring $\Delta\mathcal{R}(\text{track}, \ell) > 0.5$.

Electrons are identified in the EM calorimeter. Cells are clustered according to a cone algorithm within $\Delta\mathcal{R} < 0.2$ and then matched with an inner detector track. Electron candidates are required to deposit 90% of their energy in the EM section of the calorimeter. They must also satisfy an initial selection which includes a shower shape test (χ^2_{hmx}) with respect to the expected electron shower shape, and a calorimeter isolation requirement summing calorimeter energy within $\Delta\mathcal{R} < 0.4$ but excluding the cluster energy. To further remove backgrounds, a likelihood ($\mathcal{L}_e$)

selection is determined based on seven tracking and calorimeter parameters, including $\chi^2_{\rm hmx}$, DCA, and track isolation calculated in an annulus of $0.05 < \Delta\mathcal{R} < 0.4$ around the electron. The final electron energy calibration is determined by comparing the invariant mass of high p_T electron pairs in $Z/\gamma^* \to e^+e^-$ events with the world average value of the Z boson mass as measured by the LEP experiments [4].

In $t\bar{t}$ events, the leptons and tracks originate from the hard interaction. Therefore, we require their z positions at the closest approach to the beam axis to match that of the PV within 1 cm.

We reconstruct jets using a fixed cone algorithm [17] with a radius of 0.5. The four-momentum of a jet is measured as the sum of the four-momenta assigned to calorimeter cells inside of this cone. We select jets that have a longitudinal shower profile consistent with that of a collection of charged and neutral hadrons. We confirm jets via the electronically independent calorimeter trigger readout chain. Jets from b quarks are tagged using a neural network b jet tagging algorithm [18]. This combines the impact parameters for all tracks in a jet, as well as information about reconstructed secondary vertices in the jet. We obtain a typical efficiency of 54% for b jets with $|\eta| < 2.4$ and $p_T > 30$ GeV for a selection which accepts only 1% of light flavor (u, d, s quark or gluon) jets.

Because the b jets carry away much of the rest energy of the top quarks, it is critical for the measurement of m_t that the measurements of the energies of jets from top quark decay be well calibrated. Jet energies determined from the initial cell energies do not correspond to the energies of final state particles striking the calorimeter. As a result, a detailed calibration is applied [19,20] in the data and Monte Carlo separately. In general, the energy of all final state particles inside the jet cone, $E_j^{\rm ptcl}$, can be related to the energy measured inside the jet cone, E_j, by $E_j^{\rm ptcl} = (E_j - O)/(RS)$. Here, O denotes an offset energy primarily from extra interactions in or out of time with an event. R is the cumulative response of the calorimeter to all of the particles in a jet. S is the net energy loss due to showering out of the jet cone. For a given cone radius, O and S are functions of the jet η within the detector. O is also a function of the number of reconstructed event vertices and the instantaneous luminosity. R is the largest correction and reflects the lower response of the calorimeters to charged hadrons relative to electrons and photons. It also includes the effect of energy losses in front of the calorimeter. The primary response correction is derived *in situ* from γ + jet events and has substantial dependences on jet energy and η. For all jets that contain a nonisolated muon, we add the muon momenta to that of the jet. Under the assumption that these are b quark semileptonic decays, we also add an estimated average neutrino momentum assumed to be collinear with the jet direction. The correction procedure discussed above does not correct all the way back to the original b quark parton energy.

The event missing transverse energy, $\not\!\!E_T$, is equal in magnitude and opposite in direction to the vector sum of all significant transverse energies measured by the individual calorimeter cells. It is corrected for the transverse momenta of all isolated muons, as well as for the corrections to the electron and jet energies. In the ℓ + track channels, the $\not\!\!E_T$ is also corrected if the track does not point to a jet, electron, or muon. In this case, we substitute the track p_T for the calorimeter energy within a cone of radius $\Delta\mathcal{R} = 0.4$ around the track. A more detailed description of all particle reconstruction algorithms can be found in Ref. [21].

D. Signal and background simulation

An accurate description of the composition and kinematic properties of the selected data sample is essential to the mass measurement. Monte Carlo samples for the $t\bar{t}$ processes are generated for several test values of the top quark mass. The event generation, fragmentation, and decay are performed by PYTHIA 6.319 [22]. Background processes are called ''physics'' backgrounds when charged leptons originate from W or Z boson decay and when $\not\!\!E_T$ comes from high p_T neutrinos. Physics backgrounds include $Z/\gamma^* \to \tau\tau$ with $\tau \to e$, μ and diboson (WW, WZ, and ZZ) production. The $Z/\gamma^* \to \tau\tau$ background processes are generated with ALPGEN 2.11 [23] as the event generator and PYTHIA for fragmentation and decay. We decay hadrons with b quarks using EVTGEN [24]. To avoid double-counting QCD radiation between ALPGEN and PYTHIA, the jet-parton matching scheme of Ref. [25] is employed in ALPGEN. The diboson backgrounds are simulated with PYTHIA. We use the CTEQ6L1 [26] parton distribution function (PDF). Monte Carlo events are then processed through a GEANT-based [27] simulation of the D0 detector. In order to accurately model the effects of multiple proton interactions and detector noise, data events from random $p\bar{p}$ crossings are overlaid on the Monte Carlo events. Finally, Monte Carlo events are processed through the same reconstruction software as used for data.

In order to ensure that reconstructed objects in these samples reflect the performance of the detector in data, several corrections are applied. Monte Carlo events are reweighted by the z coordinate of the PV to match the profile in data. The Monte Carlo events are further tuned such that the efficiencies to find leptons, isolated tracks, and jets in Monte Carlo events match those determined from data. These corrections depend on the p_T and η of these objects. The jet energy calibration derived for data is applied to jets in data, and the jet energy calibration derived for simulated events is applied to simulated events. We observe a residual discrepancy between jet energies in Z + jets events in data and Monte Carlo. We apply an additional correction to jet energies in the Monte Carlo

to bring them into agreement with the data. This adjustment is then propagated into the $\not\!\!E_T$. We apply additional smearing to the reconstructed jet and lepton transverse momenta so that the object resolutions in Monte Carlo match those in data. Owing to differences in b-tagging efficiency between data and simulation, b tagging in Monte Carlo events is modeled by assigning to each simulated event a weight defined as

$$P = 1 - \prod_{i=1}^{N_{\text{jets}}} [1 - p_i(\eta, p_T, \text{flavor})], \quad (1)$$

where $p_i(\eta, p_T, \text{flavor})$ is the probability of the ith jet to be identified as originating from a b quark, obtained from data measurements. This product is taken over all jets. Instrumental backgrounds are modeled from a combination of data and simulation and are discussed in Sec. III C.

III. SELECTED EVENT SAMPLE

Events are selected for all channels by requiring either two leptons (2ℓ) or a lepton and an isolated track (ℓ + track), each with $p_T > 15$ GeV. Electrons must be within $|\eta| < 1.1$ or $1.5 < |\eta| < 2.5$; muons and tracks should have $|\eta| < 2.0$. An opposite charge requirement is applied to the two leptons or to the lepton and track. At least two jets are also required with pseudorapidity $|\eta| < 2.5$ and $p_T > 20$ GeV. We require the leading jet to have $p_T > 30$ GeV. Since neutrinos coming from W boson decays in $t\bar{t}$ events are a source of significant missing energy, a cut on $\not\!\!E_T$ is a powerful discriminant against background processes without neutrinos such as $Z/\gamma^* \to ee$ and $Z/\gamma^* \to \mu\mu$. All channels except $e\mu$ require at least $\not\!\!E_T > 25$ GeV.

A. 2ℓ selection

Our selection of 2ℓ events follows Ref. [28]. In the ee channel, events with a dielectron invariant mass $M_{ee} < 15$ GeV or $84 < M_{ee} < 100$ GeV are rejected. We require $\not\!\!E_T > 35$ GeV and $\not\!\!E_T > 45$ GeV when $M_{ee} > 100$ GeV and $15 < M_{ee} < 84$ GeV, respectively. In the $\mu\mu$ channel, we select events with $M_{\mu\mu} > 30$ GeV and $\not\!\!E_T > 40$ GeV. To further reject the $Z/\gamma^* \to \mu\mu$ background in the $\mu\mu$ channel, we require that the observed $\not\!\!E_T$ be inconsistent with arising solely from the resolutions of the measured muon momenta and jet energies.

In the $e\mu$ analysis, no cut on $\not\!\!E_T$ is applied because the main background process $Z/\gamma^* \to \tau\tau$ generates four neutrinos having moderate p_T. Instead, the final selection in this channel requires $H_T^\ell = p_T^{\ell_1} + \sum(E_T^j) > 115$ GeV, where $p_T^{\ell_1}$ denotes the transverse momentum of the leading lepton, and the sum is performed over the two leading jets. This requirement rejects the largest backgrounds for this final state: $Z/\gamma^* \to \tau\tau$ and diboson production. We require the leading jet to have $p_T > 40$ GeV.

The selection described above is derived from that used for the $t\bar{t}$ cross-section analysis. Varying the $\not\!\!E_T$ and jet p_T selections indicated that this selection minimizes the statistical uncertainty on the m_t measurement. We select 17 events in the ee channel and 13 events (12 events for MWT) in the $\mu\mu$ channel. We select 39 events in the $e\mu$ channel.

B. ℓ + track selection

The selection for the ℓ + track channels is similar to that of Ref. [21]. For the e + track channel, electrons are restricted to $|\eta| < 1.1$, and the leading jet must have $p_T > 40$ GeV. The dominant ℓ + track background arises from $Z \to ee$ and $Z \to \mu\mu$ production, so we design the event selection to reject these events.

When the invariant mass of the lepton-track pair ($M_{\ell t}$) is in the range $70 < M_{\ell t} < 110$ GeV, the $\not\!\!E_T$ requirement is tightened to $\not\!\!E_T > 35(40)$ GeV for the e + track (μ + track) channel. Furthermore, we introduce the variable $\not\!\!E_T^{Z\text{-fit}}$ that corrects the $\not\!\!E_T$ in $Z \to \ell\ell$ events for mismeasured lepton momenta. We rescale the lepton and track momenta according to their resolutions to bring $M_{\ell t}$ to the mass of the Z boson (91.2 GeV) and then use these rescaled momenta to correct the $\not\!\!E_T$. Event selection based on this variable reduces the Z background by half while providing 96% efficiency for $t\bar{t}$ events. The cuts on $\not\!\!E_T^{Z\text{-fit}}$ are always identical to those on $\not\!\!E_T$.

At least one jet is required to be identified as a b jet which provides strong background rejection for the ℓ + track channels. The m_t precision is limited by signal statistics in the observed event sample when the background is reasonably low. The above selection is a result of an optimization which minimizes the statistical uncertainty on m_t. We do this in terms of $\not\!\!E_T$, $\not\!\!E_T^{Z\text{-fit}}$, the transverse momenta of the leading two jets, and the b-tagging criteria by stepping through two or more different thresholds on these requirements. After considering all possible sets of selections, we choose the one which gives the best average expected statistical uncertainty on the m_t measurement using many pseudoexperiments. The expected statistical uncertainty varies smoothly over a 15% range while the study is sensitive to 5% changes of the average statistical uncertainty.

We explicitly veto events satisfying the selection of any of the 2ℓ channels, so the ℓ + track channels are statistically independent of the 2ℓ channels. We select eight events in the e + track channel and six events in the μ + track channel.

C. Modeling instrumental backgrounds

Backgrounds can arise from instrumental effects in which the $\not\!\!E_T$ is mismeasured. The main instrumental backgrounds for the ee, $\mu\mu$, e + track, and μ + track channels are the $Z/\gamma^* \to ee$ and $Z/\gamma^* \to \mu\mu$ processes. In these cases, apparent $\not\!\!E_T$ results from tails in jet or lepton p_T

resolutions. We use the NNLO cross section for $Z/\gamma^* \to ee$, $\mu\mu$ processes, along with the Monte Carlo-derived efficiencies to estimate these backgrounds for the ee and $\mu\mu$ channels. The Monte Carlo kinematic distributions, including the $\not\!\!E_T$, are verified to reproduce a data sample dominated by these processes. For the ℓ + track channels, we normalize Drell-Yan Monte Carlo so that the total expected event yield in a ℓ + track sample with low $\not\!\!E_T$ equals the observed event yield in the data. We observe a slightly different p_T^Z distribution for simulated $Z \to \ell\ell$ events in comparison with the data. As a result, all Z boson simulated samples, including the $Z \to \tau\tau$ physics background samples, are reweighted to the observed distribution of p_T^Z in the data [29].

Another background arises when a lepton or a track within a jet is identified as an isolated lepton or track. We utilize different methods purely in the data to estimate the level of these backgrounds for each channel. In all cases, however, we distinguish reconstructed muons and tracks as ''loose'' rather than ''tight'' by releasing the isolation criteria. We make an analogous distinction for electrons by omitting the requirement on the electron likelihood, $\mathcal{L}_e$, for loose electrons.

To determine the misidentified electron background yield in the ee and $e\mu$ channels, we fit the observed distribution of $\mathcal{L}_e$ in the data to a sum of the distributions from real isolated electrons and misidentified electrons. We determine the shape of $\mathcal{L}_e$ for real electrons from a $Z \to ee$ sample with $\not\!\!E_T < 15$ GeV. For the ee channel, we extract the shape for the misidentified electrons from a sample in which one ''tag electron'' is required to have both $\chi^2_{\rm hmx}$ and $\mathcal{L}_e$ inconsistent with being from an electron. We further require $M_{ee} < 60$ GeV or $M_{ee} > 130$ GeV and $\not\!\!E_T < 15$ GeV to reject Z and W boson events. The distribution of $\mathcal{L}_e$ is obtained from a separate ''probe electron'' in the same events. In the $e\mu$ channel, the $\mathcal{L}_e$ distribution for misidentified electrons is obtained in a sample with a nonisolated muon and $\not\!\!E_T < 15$ GeV.

To estimate the background from nonisolated muons for the $e\mu$ and $\mu\mu$ channels, we use control samples to measure the fraction of muons, f_μ, with $p_T > 15$ GeV that appear to be isolated. To enhance the heavy flavor content which gives nonisolated muons, the control samples are selected to have two muons where a ''tag'' muon is required to be nonisolated. We use another ''probe'' muon to determine f_μ. The background yield for the $e\mu$ channel is computed from the number of events having an isolated electron, a muon with no isolation requirement, and the same sign charge for the two leptons. We multiply the observed yield by f_μ.

We estimate the instrumental background for the $\mu\mu$ and ℓ + track channels by using systems of linear equations describing the composition of data samples with different loose or tight lepton and/or track selections. We relate event counts in these samples to the numbers of events with real or misidentified isolated leptons using the system of equations. These equations take as inputs the efficiencies for real or misidentified leptons and tracks to pass the tight identification requirements. For the $\mu\mu$ and ℓ + track channels, we determine the efficiencies for real leptons and tracks to pass the tight identification criteria using $Z \to ee$ and $Z \to \mu\mu$ events.

For the ℓ + track channels, the probabilities for misidentified leptons and tracks to pass the tight selection criteria are determined from multijet data samples with at least one loose lepton plus a jet. We reject the event if two leptons of the same flavor satisfy tight criteria to suppress Drell-Yan events. We also reject events with one or more tight leptons with different flavor from the loose lepton. These tight lepton vetoes allow some events with two loose leptons or a lepton and track in the sample. We further suppress resonant Z production by selecting events when $M_{\ell \rm t}$ and $M_{\ell\ell} > 100$ GeV or $M_{\ell \rm t}$ and $M_{\ell\ell} < 70$ GeV. We reject W + jets events and misreconstructed Z/γ^* events by requiring $\not\!\!E_T < 15$ GeV and $\not\!\!E_T^{\rm JES} < 25$ GeV. Here, $\not\!\!E_T^{\rm JES}$ is the missing transverse energy with only jet energy corrections and no lepton corrections. We use the latter because loose leptons no longer adhere to standard resolutions. We calculate the probability for electrons or muons to be misidentified by dividing the number of tight leptons by the number of loose leptons. For the track probability, we combine the e + jet and μ + jet samples and make the additional requirement that there be at least one loose track in the event. The tight track misidentification probability is again the number of tight tracks divided by the number of loose tracks.

To obtain samples dominated by misidentified isolated leptons for mass analysis, we select events with two loose leptons or tracks plus two jets. For the 2ℓ channels, we additionally require same sign dilepton events.

D. Composition of selected samples

The expected numbers of background and signal events in all five channels (assuming a top quark production cross section of 7.0 pb) are listed in Table I along with the observed numbers of candidates. The μ + track selection has half the efficiency of the e + track selection primarily due to the tight $\mu\mu$ veto. The expected and observed event yields agree for all channels. We do not include systematic uncertainties in the ℓ + track channels. The small backgrounds mean their uncertainties have a negligible effect on the measured m_t uncertainty.

Kinematic comparisons between data and the sum of the signal and background expectations provide checks of the content and properties of our data sample. Figure 1(a) shows the expected and observed distributions of $M_{\ell \rm t}$ in the e + track channel without the b-tag requirement and for an inverted $\not\!\!E_T$ requirement. The μ + track distribution looks similar (not shown). The mass peak at M_Z indicates the e + track sample is primarily composed of $Z \to ee$

TABLE I. Expected event yields for $t\bar{t}$ (we assume $\sigma_{t\bar{t}} = 7.0$ pb) and backgrounds and numbers of observed events for the five channels. The 2ℓ channel uncertainties include statistical as well as systematical uncertainties while the e + track and μ + track uncertainties are statistical only.

Sample	$t\bar{t}$	Diboson	Z	Multijet/W + jets	Total	Observed
$e\mu$	36.7 ± 2.4	1.7 ± 0.7	4.5 ± 0.7	2.6 ± 0.6	44.5 ± 2.7	39
ee	11.5 ± 1.4	0.5 ± 0.2	2.3 ± 0.4	0.6 ± 0.2	14.8 ± 1.5	17
$\mu\mu$	8.3 ± 0.5	0.7 ± 0.1	4.5 ± 0.4	0.2 ± 0.2	13.7 ± 0.7	13
e + track	9.4 ± 0.1	0.1 ± 0.0	0.4 ± 0.1	0.4 ± 0.1	10.3 ± 0.2	8
μ + track	4.6 ± 0.1	0.1 ± 0.0	0.7 ± 0.1	0.1 ± 0.0	5.5 ± 0.1	6

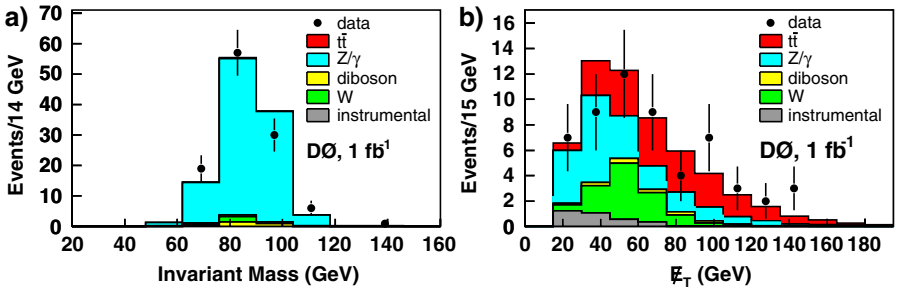

FIG. 1 (color online). Comparison of the expected distributions from individual backgrounds and $t\bar{t}$ ($m_t = 170$ GeV) in the ℓ + track channels. (a) $M_{\ell t}$ for the e + track channel without the requirement of the b tag and with inverted $\not\!\!E_T$ cuts. (b) $\not\!\!E_T$ for the sum of both ℓ + track channels, again without the b-tag requirement. We assume $\sigma_{t\bar{t}} = 7.0$ pb.

events before the final event selection. In Fig. 1(b), we show the $\not\!\!E_T$ distribution in the ℓ + track channels after all cuts except the b-tag requirement. Figures 2(a) and 2(b) show the $\not\!\!E_T$ and leading lepton p_T summed over all channels for the final candidate sample. We observe the data distributions to agree with our signal and background model.

IV. EVENT RECONSTRUCTION

Measurement of the dilepton event kinematics and constraints from the $t\bar{t}$ decay assumption allow a partial reconstruction of the final state and a determination of m_t. Given the decay of each top quark to a W boson and a b quark, with each W boson decaying to a charged lepton and a neutrino, there are six final state particles: two charged leptons, two neutrinos, and two b quarks. Each particle can be described by three momentum components. Of these 18 independent parameters, we can directly measure only the momenta of the leptons. The leading two jets most often come from the b quarks. Despite final state radiation and fragmentation, the jet momenta are highly correlated with those of the underlying b quarks. We also measure the x and y components of the $\not\!\!E_T$, $\not\!\!E_x$, and $\not\!\!E_y$, from the neutrinos. This leaves four quantities unknown. We can supply two constraints by relating the four-momenta of the leptons and neutrinos to the masses of the W bosons:

$$M_W^2 = (E_{\nu_1} + E_{l_1})^2 - (\vec{p}_{\nu_1} + \vec{p}_{l_1})^2,$$
$$M_W^2 = (E_{\nu_2} + E_{l_2})^2 - (\vec{p}_{\nu_2} + \vec{p}_{l_2})^2, \quad (2)$$

where the subscript indices indicate the $\ell\nu$ pair coming

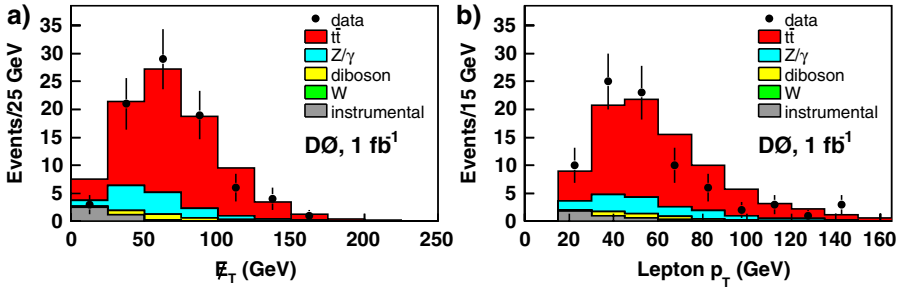

FIG. 2 (color online). (a) $\not\!\!E_T$ and (b) leading lepton p_T for $t\bar{t}$ ($m_t = 170$ GeV) and background processes overlaid with those for observed events in all channels after the final event selection. We assume $\sigma_{t\bar{t}} = 7.0$ pb.

from one or another W boson. Another constraint is supplied by requiring that the mass of the top quark and the mass of the antitop quark be equal:

$$(E_{\nu_1} + E_{l_1} + E_{b_1})^2 - (\vec{p}_{\nu_1} + \vec{p}_{l_1} + \vec{p}_{b_1})^2 = (E_{\nu_2} + E_{l_2} + E_{b_2})^2 - (\vec{p}_{\nu_2} + \vec{p}_{l_2} + \vec{p}_{b_2})^2. \quad (3)$$

The last missing constraint can be supplied by a hypothesized value of the top quark mass. With that, we can solve the equations and calculate the unmeasured top quark and neutrino momenta that are consistent with the observed event. Usually, the dilepton events are kinematically consistent with a large range of m_t. We quantify this consistency, or "weight," for each m_t by testing measured quantities of the event (e.g., $\not\!\!E_T$ or lepton and jet p_T) against expectations from the dynamics of $t\bar{t}$ production and decay. This requires us to sample from relevant $t\bar{t}$ distributions, yielding many solutions for a specific m_t. We sum the weights for each solution for each m_t. The distribution of weight vs m_t is termed a "weight distribution" of a given event. Using parameters from these weight distributions, we can then determine the most likely value of m_t.

Several previous efforts to measure m_t using dilepton events have used event reconstruction techniques. The differences between methods stem largely from which event parameters are used to calculate the event weight. We use the νWT and MWT techniques to determine the weighting as described below.

A. Neutrino weighting

The νWT method omits the measured $\not\!\!E_T$ for kinematic reconstruction. Instead, we choose the pseudorapidities of the two neutrinos from $t\bar{t}$ decay from their expected distributions. We obtain the distribution of neutrino η from several simulated $t\bar{t}$ samples with a range of m_t values. These distributions can each be approximated by a single Gaussian function. The standard deviation specifying this function varies weakly with m_t. Once the neutrino pseudorapidities are fixed and a value for m_t assumed, we can solve for the complete decay kinematics, including the unknown neutrino momenta. There may be up to four different combinations of solved neutrino momenta for each assumed pair of neutrino η values for each event. We assume the leading two jets are the b jets, so there are two possible associations of W bosons with b jets.

For each pairing of neutrino momentum solutions, we define a weight, w, based on the agreement between the measured $\not\!\!E_T$ and the sum of the neutrino momentum components in x and y, p_x^ν, and p_y^ν. We assume independent Gaussian resolutions in measuring $\not\!\!E_x$ and $\not\!\!E_y$. The weight is calculated as

$$w = \exp\left[\frac{-(\not\!\!E_x^{\text{calc}} - \not\!\!E_x^{\text{obs}})^2}{2(\sigma_x^{\text{u}})^2}\right] \exp\left[\frac{-(\not\!\!E_y^{\text{calc}} - \not\!\!E_y^{\text{obs}})^2}{2(\sigma_y^{\text{u}})^2}\right], \quad (4)$$

reflecting the agreement between the measured and calculated $\not\!\!E_T$. $\not\!\!E_i^{\text{obs}}$ ($i = x$ or y) are the components of the measured event $\not\!\!E_T$, and $\not\!\!E_i^{\text{calc}}$ are the components of the $\not\!\!E_T$ calculated from the neutrino transverse momenta resulting from each solution. We calculate the quantities $\not\!\!E_i^{\text{u}}$ to be the sums of the energies projected onto the i axes measured by all "unclustered" calorimeter cells—those cells not included in jets or electrons. The high p_T objects, leptons, and jets enter into the determination of both $\not\!\!E_i^{\text{calc}}$ and $\not\!\!E_i^{\text{obs}}$ whereas the unclustered energy $\not\!\!E_i^{\text{u}}$ only enters into $\not\!\!E_i^{\text{obs}}$. Given the resolutions σ_i^{u} of the $\not\!\!E_i^{\text{u}}$, we can therefore estimate the probability that the $\not\!\!E_i^{\text{obs}}$ are consistent with the $\not\!\!E_i^{\text{calc}}$ from the $t\bar{t}$ hypothesis.

As parameters of the method, we determine σ_i^{u} using $Z \to ee + 2$ jets data and Monte Carlo events. We calculate an unclustered scalar transverse energy, S_T^{u}, as the scalar sum of the transverse energies of all unclustered calorimeter cells. Because of the azimuthal isotropy of the calorimeter, we observe that the independent x and y components of the σ_i^{u} depend on S_T^{u} in the same way within their uncertainties. Therefore, we combine results for both components to determine our resolution more precisely. We find agreement between data and simulation in the observed dependence of these parameters on S_T^{u}. The distributions are shown for these combined resolutions in Fig. 3. We fit the unclustered $\not\!\!E_T$ resolutions obtained from simulation as

$$\sigma_x^{\text{u}}(S_T^{\text{u}}) = \sigma_y^{\text{u}}(S_T^{\text{u}}) = 4.38 \text{ GeV} + 0.52\sqrt{S_T^{\text{u}}} \text{ GeV}, \quad (5)$$

and use this parametrization for the unclustered missing energy resolution for both data and Monte Carlo in Eq. (4).

For each event, we consider ten different η assumptions for each of the two neutrinos. We extract these values from the histograms appropriate to the m_t being assumed. The ten η values are the medians of each of ten ranges of η which each represent 10% of the $t\bar{t}$ sample for a given m_t.

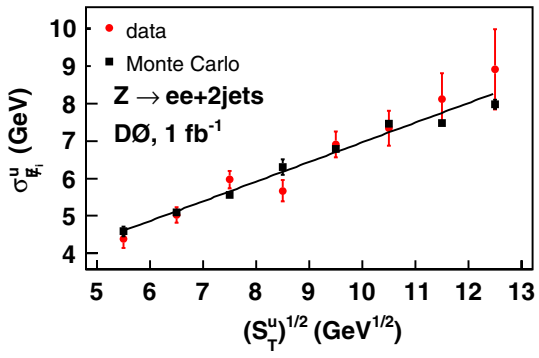

FIG. 3 (color online). Dependence of the resolution of unclustered $\not\!\!E_T$ on the unclustered scalar transverse missing energy for $Z \to ee$ events with exactly two jets.

B. Matrix weighting

In the MWT approach, we use the measured momenta of the two charged leptons. We assign the measured momenta of the two jets with the highest transverse momenta to the b and $\bar{b}$ quarks and the measured $\not\!\!E_T$ to the sum of the transverse momenta of the two neutrinos from the decay of the t and $\bar{t}$ quarks. We then assume a top quark mass and a jet assignment, and we determine the momenta of the t and $\bar{t}$ quarks that are consistent with these measurements. We refer to each such pair of momenta as a solution for the event. For each of the two jet assignments for each event, there can be up to four solutions. We assign a weight to each solution, analogous to the νWT weight of Eq. (4), given by

$$w = f(x)f(\bar{x})p(E_\ell^*|m_t)p(E_{\bar{\ell}}^*|m_t), \tag{6}$$

where $f(x)$ is the PDF for the proton for the momentum fraction x carried by the initial quark, and $f(\bar{x})$ is the corresponding value for the initial antiquark. The quantity E_ℓ^* is the observed lepton energy in the top quark rest frame. We use the central fit of the CTEQ6L1 PDFs and evaluate them at $Q^2 = m_t^2$. The quantity $p(E_\ell^*|m_t)$ in Eq. (6) is the probability that for the hypothesized top quark mass m_t, the lepton ℓ has the measured E_ℓ^* [11]:

$$p(E_\ell^*|m_t) = \frac{4m_t E_\ell^*(m_t^2 - m_b^2 - 2m_t E_\ell^*)}{(m_t^2 - m_b^2)^2 + M_W^2(m_t^2 - m_b^2) - 2M_W^4}. \tag{7}$$

C. Total weight vs m_t

Equations (4) and (6) indicate how the event weight is calculated for a given top quark mass in the νWT and MWT methods. In each method, we consider all solutions and jet assignments to get a total weight, $w_{\rm tot}$, for a given m_t. In general, there are two ways to assign the two jets to the b and $\bar{b}$ quarks. There are up to four solutions for each hypothesized value of the top quark mass. The likelihood for each assumed top quark mass m_t is then given by the sum of the weights over all the possible solutions:

$$w_{\rm tot} = \sum_i \sum_j w_{ij}, \tag{8}$$

where j sums over the solutions for each jet assignment i. We repeat this calculation for both the νWT and MWT methods for a range of assumed top quark masses from 80 GeV through 330 GeV.

For each method, we also account for the finite resolution of jet and lepton momentum measurements. We repeat the weight calculation with input values for the measured momenta (or inverse momenta for muons) drawn from normal distributions centered on the measured values with widths equal to the known detector resolutions. We then average the weight distributions obtained from N such variations:

$$w_{\rm tot}(m_t) = N^{-1} \sum_{n=1}^{N} w_{{\rm tot},n}(m_t), \tag{9}$$

where N is the number of samples. One important benefit of this procedure is that the efficiency of signal events to provide solutions increases. For instance, the νWT efficiency to find a solution for $t\bar{t} \to e\mu$ events is 95.9% without resolution sampling, while 99.5% provide solutions when $N = 150$. For the MWT analysis, events with $m_t = 175$ GeV yield an efficiency of 90% without resolution sampling. This rises to over 99% when $N = 500$. We use $N = 150$ and 500 for νWT and MWT, respectively.

Examples of single event weight distributions for νWT and MWT methods are shown in Fig. 4 for two different simulated events. The most probable fitted mass and mean fitted mass are correlated with the input m_t, yielding on average similar sensitivities for the two methods. However, there are significant event-to-event variations in the details of the weight distributions. There are also significant differences between νWT and MWT for the same event. These variations can be caused by an overall insensitivity of an event's kinematic quantities to m_t, or to a different sensitivity when using those kinematic quantities with specific event reconstruction techniques.

Properties of the weight distribution are strongly correlated with m_t if the top quark decay is as expected in the standard model. For instance, Fig. 5(a) illustrates the correlation of the mean of the νWT weight distribution, μ_w, with the generated top quark mass from the Monte Carlo. The relationship between the root-mean-square of the weight distribution, σ_w, and μ_w also varies with m_t, as shown in Fig. 5(b). There is the potential for nonstandard decays of the top quark. For $m_t = 170$ GeV and assuming BR$(H^\pm \to \tau\nu) \sim 100\%$, we observe μ_w (νWT) to shift

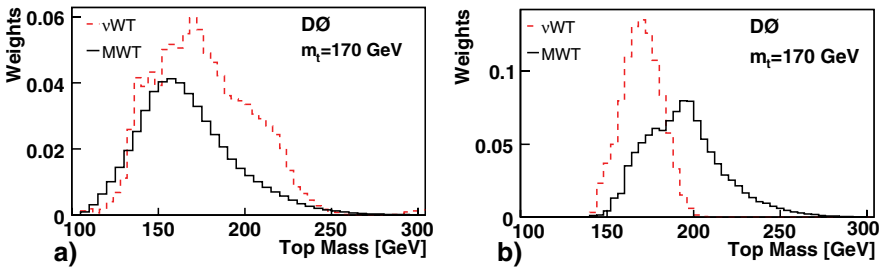

FIG. 4 (color online). Example weight distributions for two different $t\bar{t} \to e\mu$ Monte Carlo events obtained with νWT and MWT methods. The generator level mass is $m_t = 170$ GeV.

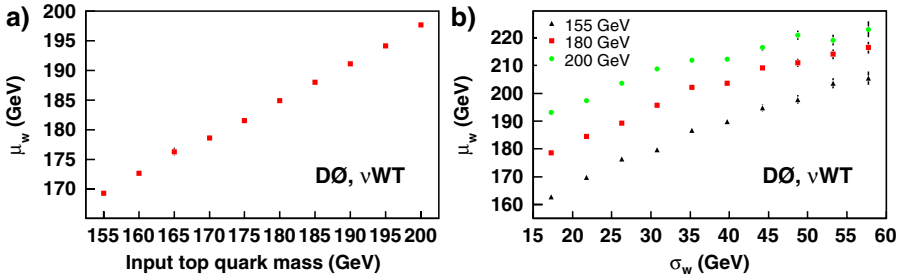

FIG. 5 (color online). (a) Correlation between the mean of the νWT weight distribution and the input m_t. (b) Correlation between νWT μ_w and σ_w for the $e\mu$ channel. Three test masses of 155 GeV, 180 GeV, and 200 GeV are shown.

systematically upward when a $H^{\pm}$ boson of mass 80 GeV is present in the decay chain instead of a W boson. When $\mathrm{BR}(t \to H^{\pm} b) = 100\%$, this shift is 10%. Thus, the measurements of this paper are strictly valid only for standard model top quark decays.

V. EXTRACTING THE TOP QUARK MASS

We cannot determine the top quark mass directly from μ_w or from the most probable mass from the event weight distributions, $\max_w$. Effects such as initial and final state radiation systematically shift these quantities from the actual top quark mass. In addition, the presence of background must be taken into account when evaluating events in the candidate sample. We therefore perform a maximum likelihood fit to distributions (''templates'') of characteristic variables from the weight distributions. The fit accounts for the shapes of signal and background templates. This section describes two different approaches to the νWT fit, and one approach for MWT.

A. Measurement using templates

We define a set of input variables characterizing the weight distribution for event i, denoted by $\{x_i\}_N$, where N is the number of variables. Examples of $\{x_i\}_N$ might be the integrated weight in bins of a coarsely binned template, or they might be the moments of the weight distribution. A probability density histogram for simulated signal events, h_s, is defined as an $(N+1)$-dimensional histogram of input top quark mass vs N variables. For background, h_b is defined as an N-dimensional histogram of the $\{x_i\}_N$. Both h_s and h_b are normalized to unity:

$$\int h_s(\{x_i\}_N \mid m_t) d\{x_i\}_N = 1, \tag{10}$$

$$\int h_b(\{x_i\}_N) d\{x_i\}_N = 1. \tag{11}$$

An example of a template for the MWT method is shown in Fig. 6, where x_i = the peak of the weight distribution $\max_w$. We measure m_t from $h_s(\{x_i\}_N, m_t)$ and $h_b(\{x_i\}_N)$ using a maximum likelihood method. For each event in a given data sample, all $\{x_i\}_N$ are found and used for the likelihood calculation. We define a likelihood $\mathcal{L}$ as

$$\mathcal{L}(\{x_i\}_N, n_b, N_{\mathrm{obs}} \mid m_t) = \prod_{i=1}^{N_{\mathrm{obs}}} \frac{n_s h_s(\{x_i\}_N \mid m_t) + n_b h_b(\{x_i\}_N)}{n_s + n_b}, \tag{12}$$

where N_{obs} is the number of events in the sample, n_b is the number of background events, and n_s is the signal event yield. We obtain a histogram of $-\ln\mathcal{L}$ vs m_t for the sample. We fit a parabola that is symmetric around the point with the highest likelihood (lowest $-\ln\mathcal{L}$). The fitted mass range is several times larger than the expected statistical uncertainty. It is chosen *a priori* to give the best sensitivity to the top quark mass using Monte Carlo pseudoexperiments, and is typically around ± 20 GeV.

We obtain measurements of m_t for several channels by multiplying the likelihoods of these channels:

$$-\ln\mathcal{L} = \sum_{\mathrm{ch}} (-\ln\mathcal{L}_{\mathrm{ch}}), \tag{13}$$

where ''ch'' denotes the set of channels. In this paper, we calculate overall likelihoods for the 2ℓ subset, ch $\in \{e\mu, ee, \mu\mu\}$; the ℓ + track subset, ch $\in \{e$ + track, μ + track$\}$; and the five channel dilepton set, ch $\in \{e\mu, ee, \mu\mu, e$ + track, μ + track$\}$.

B. Choice of template variables

The choice of variables characterizing the weight distributions has been given some consideration in the past.

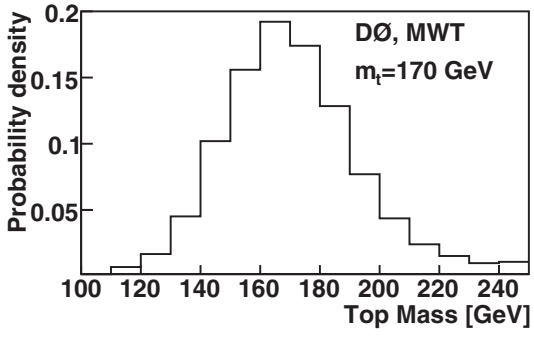

FIG. 6. An example of a template for the MWT method.

For example, the D0 MWT analysis and CDF νWT analyses have used $\max_w$ [14,15]. Earlier D0 νWT analyses employed a multiparameter probability density technique using the coarsely binned weight distribution to extract a measure of m_t [13,14].

For the MWT analysis described here, we use the single parameter approach. In particular, to extract the mass, we use Eq. (12) where $x_i = \{\max_w\}$. We determine the values of n_s and n_b by scaling the sum of the expected numbers of signal ($\bar{n}_s$) and background ($\bar{n}_b$) events in Table I to the number observed in each channel. We fit the histogram of $-\ln\mathcal{L}$ to a parabola using a 40 GeV wide mass range centered at the top quark mass with the minimal value of $-\ln\mathcal{L}$ for all channels.

For the νWT analysis, we define the optimal set of input variables for the top quark mass extraction to be the set that simultaneously minimizes the expected statistical uncertainty and the number of variables. The coarsely binned weight distribution approach exhibits up to 20% better statistical performance than single parameter methods for a given kinematic reconstruction approach by using more information. However, over five bins are typically needed, and the large number of variables and their correlations significantly complicate the analysis. We study the performance of the method with many different choices of variables from the weight distributions. These include single parameter choices such as $\max_w$ or μ_w, which provide similar performance in the range 140 GeV $< m_t <$ 200 GeV.

Vectors of multiple parameters included various coarsely binned templates, or subsets of their bins. For the νWT analysis, we observe that individual event weight distributions have fluctuations which are reduced by considering bulk properties such as their moments. The most efficient parameters are the first two moments (μ_w and σ_w) of the weight distribution. This gives 16% smaller expected statistical uncertainty than using $\max_w$ or μ_w alone. The improvement of the performance comes from the fact that σ_w is correlated with μ_w for a given input top quark mass. This is shown in Fig. 5(b) for three different input top quark masses. The value of σ_w helps to better identify the range of input m_t that is most consistent with the given event having a specific μ_w. This ability to deweight incorrect m_t assignments results in a narrower likelihood distribution and causes a corresponding reduction in the statistical uncertainty. No other choice of variables gives significantly better performance. The method that uses the weight distribution moments, $x_i = \{\mu_w, \sigma_w\}$, in histograms h_s and h_b with Eq. (12) is termed $\nu\mathrm{WT}_h$.

Because the templates are two dimensional for background and three-dimensional for signal, a small number of bins are unpopulated. We employ a constant extrapolation for unpopulated edge bins using the value of the populated bin closest in m_t but having the same μ_w and σ_w. For empty bins flanked by populated bins in the m_t direction but with the same μ_w and σ_w, we employ a linear interpolation. We fit the histogram of $-\ln\mathcal{L}$ vs m_t with a parabola. When performing the fit, the $\nu\mathrm{WT}_h$ approach determines n_s to be $n_s = N_{\mathrm{obs}} - \bar{n}_b$. Fit ranges of 50, 40, and 30 GeV are used for ℓ + track, 2ℓ, and all dilepton channels, respectively.

C. Probability density functions

In both methods described above, there are finite statistics in the simulated samples used to model h_s and h_b, leading to bin-by-bin fluctuations. We address this in the νWT analysis by performing fits to h_s and h_b templates. We term this version of the νWT method $\nu\mathrm{WT}_f$. For the signal, we generate a probability density function f_s by fitting h_s with the functional form

$$\begin{aligned} f_s(\mu_w, \sigma_w \mid m_t) &= (\sigma_w + p_{13})^{p_6} \exp[-p_7(\sigma_w + p_{13})^{p_8}] \\ &\times \left\{(1 - p_9)\frac{1}{\sigma\sqrt{2\pi}} \exp\left[-\frac{(\mu_w - m)^2}{2\sigma^2}\right]\right. \\ &+ p_9 \cdot \frac{p_{11}^{1+p_{12}}}{\Gamma(1 + p_{12})}\left(\mu_w - \frac{m}{p_{10}}\right)^{p_{12}} \\ &\times \left.\exp\left[-p_{11}\left(\mu_w - \frac{m}{p_{10}}\right)\right]\Theta\left(\mu_w - \frac{m}{p_{10}}\right)\right\} \\ &\times \left\{\int_0^\infty (x + p_{13})^{p_6} \exp[-p_7(x + p_{13})^{p_8}]dx\right\}^{-1}. \end{aligned} \quad (14)$$

The parameters m and σ are linear functions of σ_w and m_t:

$$\begin{aligned} m &= p_0 + p_1(\sigma_w - 36\ \mathrm{GeV}) + p_2(m_t - 170\ \mathrm{GeV}), \\ \sigma &= p_3 + p_4(\sigma_w - 36\ \mathrm{GeV}) + p_5(m_t - 170\ \mathrm{GeV}). \end{aligned} \quad (15)$$

Equations (14) and (15) are *ad hoc* functions determined empirically. A typical χ^2 with respect to h_s is found in the $e\mu$ channel which yields 4.0 per degree of freedom. The linear relationship between σ_w and μ_w is shown in Fig. 7(a), which is an example of the probability density vs σ_w and μ_w for fixed input top quark mass of 170 GeV. The dependence of f_s on σ_w is expressed in the first line of Eq. (14). The second and third lines contain a Gaussian plus an asymmetrical function to describe the dependence on μ_w. The factors $1/(\sigma\sqrt{2\pi})$ and $p_{11}^{1+p_{12}}/\Gamma(1 + p_{12})$ and the integral in the fourth line normalize the probability density function to unity. Examples of two-dimensional slices of three-dimensional signal histograms for fixed input $m_t = 170$ GeV and $\sigma_w = 30$ GeV are shown in Fig. 7(a) and 7(c), respectively. The corresponding slices of the fit functions are shown in Fig. 7(b) and 7(d), respectively.

The background probability density function $f_b(\mu_w, \sigma_w)$ is obtained as the normalized two-dimensional function of μ_w and σ_w of simulated background events:

$$f_b(\mu_w, \sigma_w) = \frac{\exp[-(p_1\mu_w + p_2\sigma_w - p_0)^2 - (p_4\mu_w + p_5\sigma_w - p_3)^2]}{\int_0^\infty \int_0^\infty \exp[-(p_1 x + p_2 y - p_0)^2 - (p_4 x + p_5 y - p_3)^2]dxdy}. \quad (16)$$

This is also an *ad hoc* function determined empirically. The fit is performed to h_b containing the sums of all backgrounds for each channel and according to their expected yields. A typical χ^2 with respect to h_b is found in the $e\mu$ case which yields 5.2 per degree of freedom. Examples of h_b and f_b are shown in Fig. 8(a) and 8(b), respectively.

To measure m_t, we begin by adding two extra terms to the likelihood $\mathcal{L}$ of Eq. (12). The first term is a constraint that requires that the fitted sum of the number of signal events n_s and the number of background events n_b agrees within Poisson fluctuations with the number of observed events $N_{\rm obs}$:

$$\mathcal{L}_{\rm poisson}(n_s + n_b, N_{\rm obs}) \equiv \frac{(n_s + n_b)^{N_{\rm obs}} \exp[-(n_s + n_b)]}{N_{\rm obs}!}. \quad (17)$$

The second term is a Gaussian constraint that requires agreement between the fitted number of background events n_b and the number of expected background events $\bar{n}_b$ within Gaussian fluctuations, where the width of the Gaussian is given by the estimated uncertainty δ_b on $\bar{n}_b$:

$$\mathcal{L}_{\rm gauss}(n_b, \bar{n}_b, \delta_b) \equiv \frac{1}{\sqrt{2\pi}\delta_b} \exp[-(n_b - \bar{n}_b)^2/2\delta_b^2]. \quad (18)$$

The total likelihood for an individual channel is given by

$$\mathcal{L}(\mu_{wi}, \sigma_{wi}, \bar{n}_b, N_{\rm obs} \mid m_t, n_s, n_b) = \mathcal{L}_{\rm gauss}(n_b, \bar{n}_b, \delta_b)\mathcal{L}_{\rm poisson}(n_s + n_b, N_{\rm obs}) \times \prod_{i=1}^{N_{\rm obs}} \frac{n_s f_s(\mu_{wi}, \sigma_{wi} \mid m_t) + n_b f_b(\mu_{wi}, \sigma_{wi})}{n_s + n_b}. \quad (19)$$

The product extends over all events in the data sample. The maximum of the likelihood corresponds to the measured top quark mass. We simultaneously minimize $-\ln\mathcal{L}$ with respect to m_t, n_s, and n_b using MINUIT [30,31]. The fitted sample composition is consistent with the expected one. We obtain the statistical uncertainty by considering the analytic function of $-\ln\mathcal{L}$ vs m_t, n_s, and n_b near the most likely point. The matrix of second derivatives at this point is inverted, and the result provides the parameter uncertainties such that their correlations are taken into account. This works because the $-\ln\mathcal{L}$ is nearly quadratic in n_s, n_b, and m_t near the minimum. We obtain measurements of m_t for several channels by minimizing the combined $-\ln\mathcal{L}$ simultaneously with respect to m_t and the numbers of signal and background events for the channels considered.

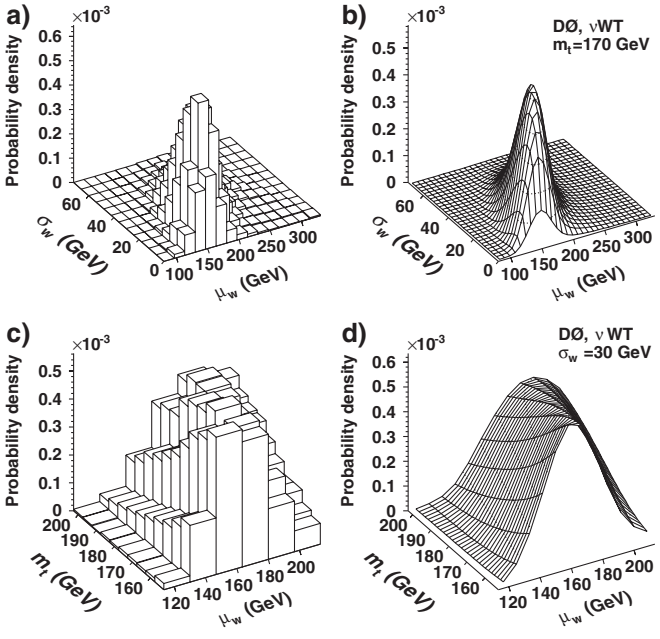

FIG. 7. Slices of probability density histograms h_s and fit functions f_s for the νWT method in the $e\mu$ channel. Probability densities vs σ_w and μ_w for $m_t = 170$ GeV are shown for (a) h_s and (b) f_s. Probability densities vs m_t and μ_w for $\sigma_w = 30$ GeV are shown for (c) h_s and (d) f_s.

D. Pseudoexperiments and calibration

The maximum likelihood fits attempt to account for the presence of background and for the signal and background shapes of the templates. For a precise measurement of m_t, we must test for any residual effects that can cause a shift in the relationship between the fitted and actual top quark masses. We test our fits and extract correction factors for any observed shifts by performing pseudoexperiments.

A pseudoexperiment for each channel is a set of simulated events of the same size and composition as the selected data set given in Table I. We compose it by randomly drawing simulated events out of the large Monte Carlo event pool. Within a given pool, each Monte Carlo event has a weight based on production information and detector performance parameters. An example of the latter is the b-tagging efficiency which depends on jet p_T and η, and an example of the former is the weight with which each event is generated by ALPGEN. We choose a random event, and then accept or reject it by comparing the event weight to a random number. In this way, our pseudoexperiments are constructed with the mix of events that gives the correct kinematic distributions.

For MWT, we compose pseudoexperiments by drawing Monte Carlo events from signal and background samples with probabilities proportional to the numbers of events expected, $\bar{n}_s$ and $\bar{n}_b$. Thus, we draw events for each source based on a binomial probability. In the νWT pseudoexperiments, the number of background events of each source is

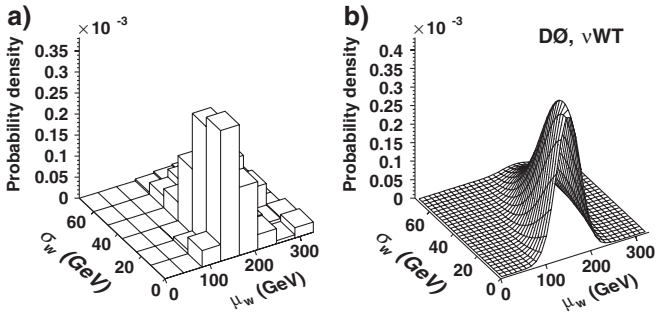

FIG. 8. Probability density histogram h_b and fit function f_s for the νWT method in the $e\mu$ channel. Probability densities vs σ_w and μ_w are shown for (a) h_b and (b) f_b.

Poisson fluctuated around the expected yields of Table I. The remaining events in the pseudoexperiment are signal events. If the sum of backgrounds totals more than N_{obs}, then the extra events are dropped and $n_s = 0$. In this way, we do not use the $t\bar{t}$ production cross section, which is a function of m_t.

To establish the relationship between the fitted top quark mass, m_t^{fit}, and the actual generated top quark mass m_t, we assemble a set of many pseudoexperiments for each input mass. For the νWT method, we use 300 pseudoexperiments. Using more pseudoexperiments would lead to excessive correlation among them, given our available Monte Carlo statistics. We average m_t^{fit} for each input m_t for each channel. We combine channels according to Eq. (13), and we fit the dependence of this average mass on m_t with

$$\langle m_t^{\text{fit}} \rangle = \alpha(m_t - 170\ \text{GeV}) + \beta + 170\ \text{GeV}. \quad (20)$$

The calibration points and fit functions are shown in Fig. 9. The results of the fits are summarized in Table II. Ideally, α and β should be unity and zero, respectively. The m_t^{fit} of each pseudoexperiment and data measurement is corrected for the slopes and offsets given in Table II by

$$m_t^{\text{meas}} = \alpha^{-1}(m_t^{\text{fit}} - \beta - 170\ \text{GeV}) + 170\ \text{GeV}. \quad (21)$$

The pull is defined as

$$\text{pull} = \frac{m_t^{\text{meas}} - m_t}{\sigma(m_t^{\text{meas}})}, \quad (22)$$

where $\sigma(m_t^{\text{meas}}) = \alpha^{-1}\sigma(m_t^{\text{fit}})$ is the measured statistical uncertainty after the calibration of Eq. (21). The ideal pull distribution has a Gaussian shape with a mean of zero and a

TABLE II. Slope (α) and offset (β) from the linear fit in Eq. (20) to the pseudoexperiment results of Fig. 9 for the 2ℓ, ℓ + track, and combined dilepton channel sets using the MWT and νWT methods.

Method	Channel	Slope: α	Offset: β [GeV]	Pull width	Expected statistical uncertainty [GeV]
νWT_h	2ℓ	0.98 ± 0.01	-0.04 ± 0.11	1.02 ± 0.02	5.8
νWT_h	ℓ + track	0.92 ± 0.02	2.28 ± 0.27	1.04 ± 0.02	13.0
νWT_h	combined	0.99 ± 0.01	-0.04 ± 0.11	1.03 ± 0.02	5.1
νWT_f	2ℓ	1.03 ± 0.01	-0.32 ± 0.15	1.06 ± 0.02	5.8
νWT_f	ℓ + track	1.07 ± 0.03	-0.04 ± 0.37	1.07 ± 0.02	12.9
νWT_f	combined	1.04 ± 0.01	-0.45 ± 0.13	1.06 ± 0.02	5.3
MWT	2ℓ	1.00 ± 0.01	0.95 ± 0.05	0.98 ± 0.01	6.3
MWT	ℓ + track	0.99 ± 0.01	0.64 ± 0.12	1.06 ± 0.01	13.8
MWT	combined	0.99 ± 0.01	0.97 ± 0.05	0.99 ± 0.01	5.8

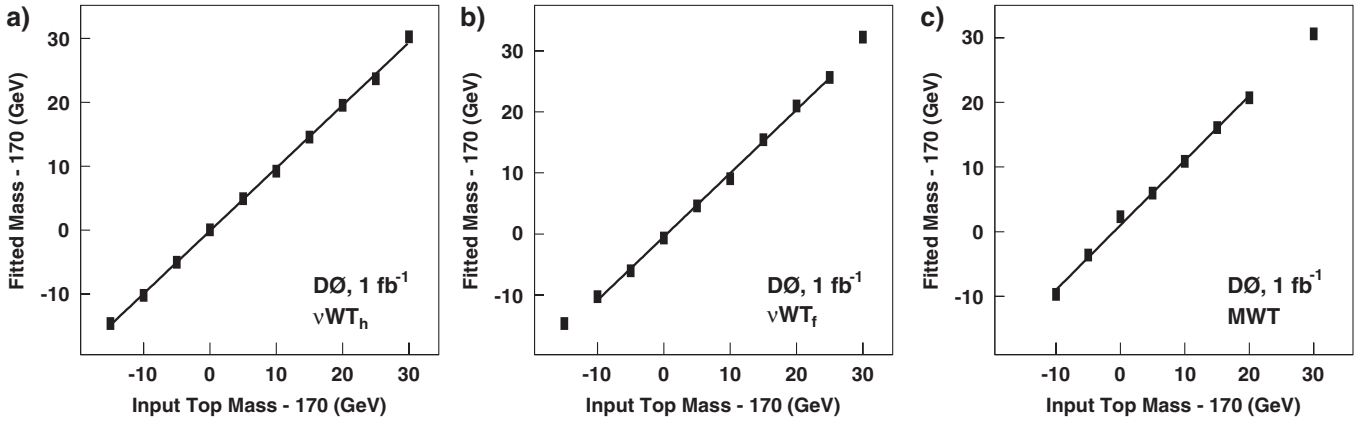

FIG. 9. The combined calibration curves corresponding to the (a) νWT_h, (b) νWT_f, and (c) MWT methods. Overlaid is the result of the linear fit as defined in Eq. (20). The uncertainties are small and corresponding bars are hidden by the markers.

width of one. The pull widths from pseudoexperiments are given in Table II. A pull width larger (less) than one indicates an underestimated (overestimated) statistical uncertainty. The uncertainty of the data measurement is corrected for deviations of the pull width from one as well as for the slope of the calibration curve. The mean of the distribution of calibrated and pull-corrected statistical uncertainties yields the expected statistical uncertainty (see Table II). Figure 10 shows the pull-width–corrected distribution of statistical uncertainties for the m_t measurements from the ensemble testing. The expected uncertainty on the combined measurement for all channels is 5.1, 5.3, and 5.8 GeV for $\nu\mathrm{WT}_h$, $\nu\mathrm{WT}_f$, and MWT, respectively.

VI. RESULTS

The calibrated mass and statistical uncertainties for the 2ℓ, ℓ + track, and their combination are shown in Table III for each of the three methods. The $-\ln\mathcal{L}$ fits from the $\nu\mathrm{WT}_h$, $\nu\mathrm{WT}_f$, and MWT methods, including data points, are shown in Fig. 11. There are no data points for the $\nu\mathrm{WT}_f$ fit since the corresponding curve is a one-dimensional slice of an analytic three-dimensional fit function, f_s. The calibrated statistical uncertainties determined in the data from these likelihood curves are shown by arrows in Fig. 10. The statistical uncertainties agree with the expectations from ensemble testing.

A. Systematic uncertainties

The top quark mass measurement relies substantially on the Monte Carlo simulation of $t\bar{t}$ signal and backgrounds. While we have made adjustments to this model to account for the performance of the detector, residual uncertainties remain. The limitations of modeling of physics processes may also affect the measured mass. There are several categories of systematic uncertainties: modeling of physics processes, modeling of the detector response, and the method. We have estimated each of these as follows.

TABLE III. Calibrated fitted m_t for the $\nu\mathrm{WT}_h$, $\nu\mathrm{WT}_f$, and MWT methods. All uncertainties are statistical.

Channel	$\nu\mathrm{WT}_h$ [GeV]	$\nu\mathrm{WT}_f$ [GeV]	MWT [GeV]
2ℓ	177.5 ± 5.5	176.1 ± 5.8	176.6 ± 5.5
ℓ + track	170.7 ± 12.3	174.6 ± 13.8	165.0 ± 8.5
Combined	176.3 ± 4.9	176.0 ± 5.3	173.2 ± 4.9

1. Physics modeling

(a) *b fragmentation.*—A systematic uncertainty arises from the different models of b quark fragmentation, namely, the distribution of the fraction of energy taken by the heavy hadron. The standard D0 simulation used for this analysis utilizes the default PYTHIA tune in the Bowler scheme [32]. We reweight our $t\bar{t}$ simulated samples to reach consistency with the fragmentation model measured in $e^+e^- \to Z \to b\bar{b}$ decays [33]. A systematic uncertainty is assessed by comparing the measured m_t in these two scenarios.

(b) *Underlying event model.*—An additional systematic uncertainty can arise from the underlying event model. We compare measured top quark masses for the PYTHIA tune DW [34] with the nominal model (tune A) [35]. Tune DW refers to the set of PYTHIA parameters that were tuned to fit

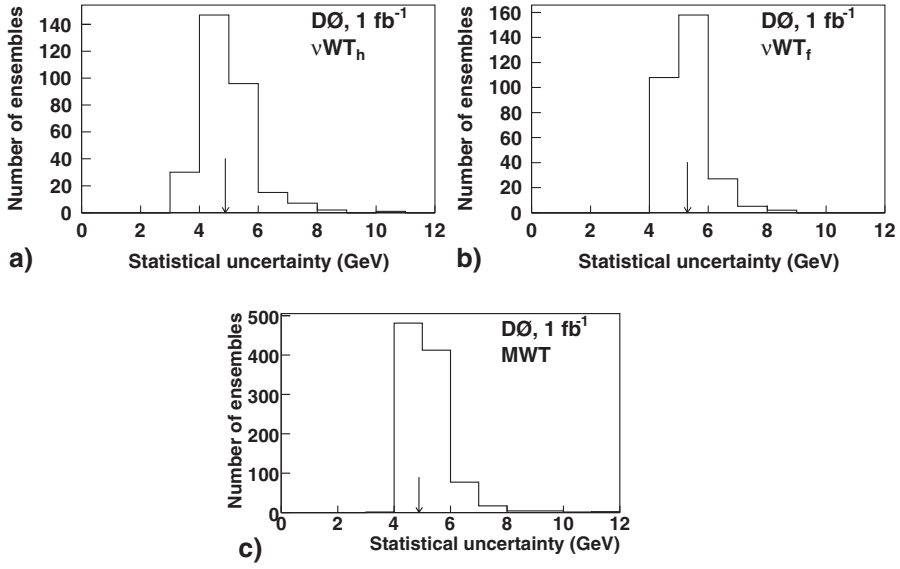

FIG. 10. Distribution of statistical uncertainties for top quark mass measurements of pseudoexperiments for the combination of all channels for simulated events with $m_t = 170$ GeV for the (a) $\nu\mathrm{WT}_h$, (b) $\nu\mathrm{WT}_f$, and (c) MWT methods. The uncertainties are corrected by the calibration curve and for the pull width. The arrows indicate the statistical uncertainties for the measured top quark mass.

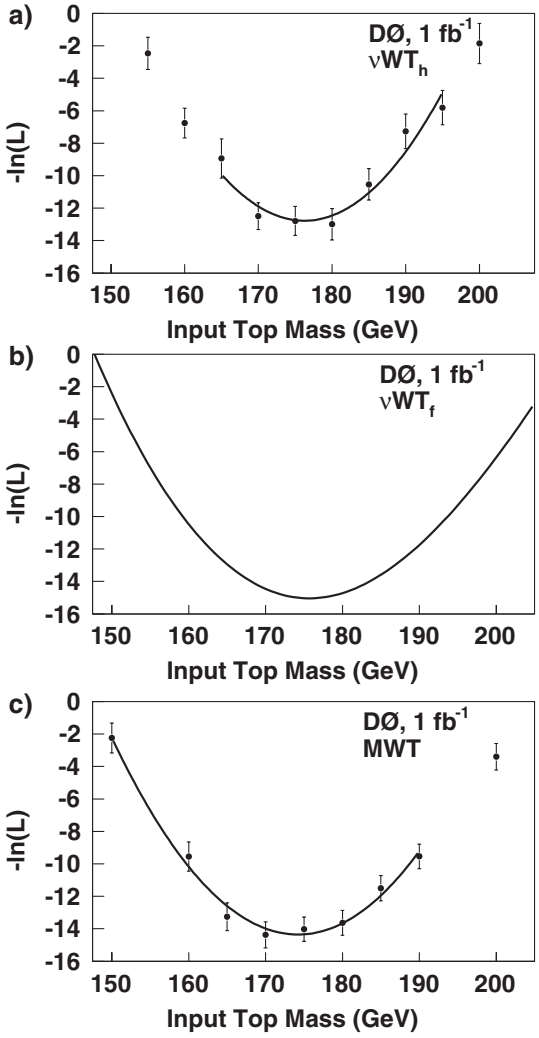

FIG. 11. Negative log-likelihood $-\ln\mathcal{L}$ vs m_t for the combination of all channels before calibration for the (a) $\nu\mathrm{WT}_h$, (b) $\nu\mathrm{WT}_f$, and (c) MWT methods.

the CDF data on dilepton (Drell-Yan) production and the jet azimuthal decorrelation in D0 dijet data [36].

(c) *Extra jet modeling*.—Extra jets in top quark events from gluon radiation can affect the $t\bar{t}$ p_T spectrum, and therefore the measured m_t. While our models describe the data within uncertainties for all channels, the ratio of the number of events with only two jets to those with three or more jets is typically four in the Monte Carlo and three in the data. To assess the effect of this difference, we reweight the simulated events with a top quark mass of 170 GeV so that this ratio is the same. Pseudoexperiments with reweighted events are compared to the nominal pseudoexperiments to determine the uncertainty.

(d) *Event generator*.—There is an uncertainty in event kinematics due to the choice of the event generator. This can lead to an uncertainty in the measured top quark mass. To account for variations in the accuracy of $t\bar{t}$ generators, we compare pseudoexperiment results using $t\bar{t}$ events generated with ALPGEN to those generated with PYTHIA for $m_t = 170$ GeV. The difference between the mean fitted mass over 300 pseudoexperiments is corrected by subtracting in quadrature the component due to the statistical independence of generator event samples.

(e) *PDF variations*.—The top quark mass measurement relies on Monte Carlo events generated with a particular PDF set (CTEQ6L1). Moreover, this PDF set is used directly by the MWT method. We estimate the resulting uncertainty on m_t by reweighting the Monte Carlo according to the different eigenvectors of the CTEQ6L1 PDFs. For each choice, we measure a new mass and the difference between the mass obtained with reweighting and a nominal mass is computed. The resulting uncertainty is the sum in quadrature of all above uncertainties.

(f) *Background template shape*.—The uncertainties on the background kinematics can affect the template shapes and consequently the measured top quark mass. The uncertainty from the background template shape is found by substituting simulated WW events for all Z backgrounds (including $Z \to \tau\tau$) in all pseudoexperiments. The uncertainty is taken as the difference between the average measured top quark mass with this assumption and the nominal value.

2. Detector modeling

(a) *Jet energy scale*.—Because the b jets carry the largest share of the energy in top quark events, their calibration has the largest effect on the uncertainty on m_t. Ideally, the procedure to calibrate jet energies in the data and Monte Carlo achieves the same energy scale in both. However, each procedure has a systematic uncertainty. We estimate the resulting uncertainty in m_t by repeating the pseudoexperiments with simulated events in which the jet energies are shifted up and down by the known p_T- and η-dependent uncertainty, obtained by summing in quadrature uncertainties on the data and Monte Carlo jet energy scales. The probability density histograms (h_s, h_b) and functions (f_s, f_b) are left with the nominal calibration.

(b) *b/light quark response ratio*.—This uncertainty arises from the fact that the jets in signal events are primarily b jets. These have a different detector response than the light quark and gluon jets which dominate the γ + jet sample used to derive the overall jet energy calibration. By applying this calibration to the b jet sample, a 1.8% shift in jet p_T is observed [37]. We adjust the jets in the Monte Carlo for this and propagate the correction into the $\not\!\!E_T$. This causes a shift in the measured m_t which is taken as an uncertainty.

(c) *Sample dependent jet energy scale*.—After the initial calibration, a residual shift in jet p_T distributions is observed in Z + jets events when comparing the data and Monte Carlo. We adopt a further calibration that improves agreement in these distributions and apply it to all of our

background samples. Because this correction may not apply to $t\bar{t}$ events, we take the shift in the measured m_t to be a systematic uncertainty.

(d) *Object resolution*.—The jet resolution from the simulation is better than that observed in the data. To improve the agreement, we apply an additional smearing to Monte Carlo events. A residual difference between the data and Monte Carlo jet resolutions can lead to a mass bias. To estimate the effect on the m_t measurement, we repeat the pseudoexperiments by adjusting this smearing up and down within its uncertainty while keeping h_s and h_b with the nominal resolutions. We estimate the systematic uncertainties arising from the muon, isolated track, and electron p_T resolutions in a similar way.

(e) *Jet identification*.—The jet reconstruction and identification efficiency in the Monte Carlo is corrected to match the data. We propagate the uncertainty on the correction factor to the top quark mass measurement.

(f) *Monte Carlo corrections*.—Residual uncertainties on the Monte Carlo corrections exist for triggering, luminosity profiles, lepton identification, and b-tagging. These uncertainties affect the top quark mass uncertainties. In each case, a respective systematic uncertainty on m_t is found by reweighting events according to the uncertainties of Monte Carlo correction factors introduced to reproduce the data.

3. Method

(a) *Background yield*.—Because of the limited statistics of the simulation, there is some uncertainty in the event yields for the background processes. This uncertainty affects the likelihood and the measured top quark mass via Eq. (12). To estimate the effect of the uncertainty on the background event yield, we vary the total background yield by its known uncertainty up and down keeping the relative ratios of individual background processes constant.

(b). *Template statistics*.—The templates used in the MWT and $\nu\mathrm{WT}_h$ methods have finite statistics. Local fluctuations in these templates can cause local fluctuations in the individual likelihood fits and the top quark mass. We obtain an uncertainty in m_t by varying the $-\ln\mathcal{L}$ points from the data ensemble within their errors. The width of the m_t distribution provides the systematic uncertainty.

For the $\nu\mathrm{WT}_f$ method, the f_s function depends on 15 parameters, each of which has a corresponding uncertainty. Consequently, there is some uncertainty on the shape of this function. There is a corresponding uncertainty on the parameters of the f_b. The uncertainty on the shape causes the fit uncertainty on the measured top quark mass. We find the impact of this uncertainty on the data sample by varying the parameters of f_s and f_b within their uncertainties. For each such variation, we remeasure m_t for the data sample. The fit uncertainty is the width of this distribution.

(c) *Monte Carlo calibration*.—There is an uncertainty on fitting the parameters (slope and offset) of the calibration curve. This uncertainty causes an uncertainty in the calibrated top quark mass. The calibration uncertainty is obtained as the uncertainty of the offset.

A summary of estimated systematic errors for the combined dilepton channels is provided in Table IV. We assume the systematic uncertainties for all three methods to be completely correlated for each source of systematic uncertainty and uncorrelated among different sources. The correlations of statistical uncertainties are given in the next section. All uncertainties are corrected for the slope of the mass scale calibration. The total uncertainty is found by assuming all the contributions are independent and adding them in quadrature.

B. Combined results

The statistical use of the νWT moments template is different between the $\nu\mathrm{WT}_h$ and $\nu\mathrm{WT}_f$ methods. This is primarily due to the differences between histogram and fit function shapes indicated by the high $\chi^2/\mathrm{d.o.f.}$ in Sec. V C. Nevertheless, both approaches show similar performance on average, as illustrated in Table II. Pseudoexperiment tests show that these two measurements are only 85% correlated. These tests also reveal that the width (root-mean-squared, or fitted Gaussian σ) of the mass calculated from a combination of the two methods using the best linear unbiased estimator method [38] is reduced by several percent. The estimated, calibrated statistical uncertainty reduces by a similar amount. We therefore apply the correlation to the measurements from data and obtain a final νWT measurement of $m_t = 176.2 \pm 4.8(\mathrm{stat}) \pm 2.1(\mathrm{sys})$ GeV for the combination of all five channels. We treat all systematic uncertainties as 100% correlated across methods except for the Monte Carlo calibration and template statistics uncertainties. These are treated as uncorrelated and 85% correlated, respectively. The individual systematic uncertainties on the νWT combination are determined to equal those for the $\nu\mathrm{WT}_h$ method to the precision given in Table IV.

The final MWT measurement is $m_t = 173.2 \pm 4.9(\mathrm{stat}) \pm 2.0(\mathrm{sys})$ GeV for the combination of all dilepton channels. The total systematic uncertainties are 2.0 GeV and 2.4 GeV for the 2ℓ and ℓ + track MWT results, respectively. The νWT and MWT approaches use partially different information from each $t\bar{t}$ event; the two results are measured to be 61% correlated. Therefore, we use the best linear unbiased estimator method to determine an overall measurement of $m_t = 174.7 \pm 4.4(\mathrm{stat}) \pm 2.0(\mathrm{sys})$ GeV for the combination of all dilepton channels. We treat all systematic uncertainties as 100% correlated across methods except for two uncertainties. The Monte Carlo calibration and template statistics systematic uncertainties are treated as uncorrelated and 61% correlated, respectively. The channel-specific results for both measurement combinations are given in Table V.

TABLE IV. Summary of systematic uncertainties for the combined analysis of all dilepton channels. The νWT$_h$, νWT$_f$, and MWT method results are shown.

Source of uncertainty	νWT$_h$ [GeV]	νWT$_f$ [GeV]	MWT [GeV]
b fragmentation	0.4	0.5	0.4
Underlying event modeling	0.3	0.1	0.5
Extra jets modeling	0.1	0.1	0.3
Event generator	0.5	0.7	0.5
PDF variation	0.2	0.3	0.5
Background template shape	0.4	0.3	0.3
Jet energy scale (JES)	1.5	1.6	1.2
b/light response ratio	0.3	0.4	0.6
Sample dependent JES	0.4	0.4	0.1
Jet energy resolution	0.1	0.1	0.2
Muon/track p_T resolution	0.1	0.1	0.2
Electron energy resolution	0.1	0.2	0.2
Jet identification	0.4	0.5	0.5
MC corrections	0.2	0.3	0.2
Background yield	0.0	0.1	0.1
Template statistics	0.8	1.0	0.8
MC calibration	0.1	0.1	0.1
Total systematic uncertainty	2.1	2.3	2.0

TABLE V. Final results for the νWT method and νWT + MWT combination.

Channel	νWT [GeV]	νWT + MWT [GeV]
2ℓ	177.1 ± 5.4(stat) ± 2.0(sys)	176.9 ± 4.8(stat) ± 1.9(sys)
ℓ + track	171.2 ± 12.3(stat) ± 2.7(sys)	165.7 ± 8.4(stat) ± 2.4(sys)
Combined	176.2 ± 4.8(stat) ± 2.1(sys)	174.7 ± 4.4(stat) ± 2.0(sys)

VII. CONCLUSIONS

In 1 fb^{-1} of $p\bar{p}$ collision data from the Fermilab Tevatron collider, we employed two mass extraction methods to measure m_t in $t\bar{t}$ events with two high p_T final state leptons. We analyzed three channels with two fully identified leptons ($e\mu$, ee, and $\mu\mu$) and two channels with relaxed lepton selection and a b-tagged jet (e + track and μ + track). Using the νWT event reconstruction, we perform a maximum likelihood fit to the first two moments of the resulting distribution of relative weight vs m_t to measure

$$m_t = 176.2 \pm 4.8(\text{stat}) \pm 2.1(\text{sys})\ \text{GeV}. \quad (23)$$

We also employ the MWT method using a fit to the mass giving the maximum weight. We measure

$$m_t = 173.2 \pm 4.9(\text{stat}) \pm 2.0(\text{sys})\ \text{GeV}. \quad (24)$$

Accounting for correlations in these two measurements, we obtain a final combined result of

$$m_t = 174.7 \pm 4.4(\text{stat}) \pm 2.0(\text{sys})\ \text{GeV}. \quad (25)$$

Our result is consistent with the current world average value of m_t [39].

ACKNOWLEDGMENTS

We thank the staffs at Fermilab and collaborating institutions, and acknowledge support from the DOE and NSF (U.S.); CEA and CNRS/IN2P3 (France); FASI, Rosatom, and RFBR (Russia); CNPq, FAPERJ, FAPESP, and FUNDUNESP (Brazil); DAE and DST (India); Colciencias (Colombia); CONACyT (Mexico); KRF, and KOSEF (Korea); CONICET and UBACyT (Argentina); FOM (The Netherlands); STFC (United Kingdom); MSMT and GACR (Czech Republic); CRC Program, CFI, NSERC, and WestGrid Project (Canada); BMBF and DFG (Germany); SFI (Ireland); The Swedish Research Council (Sweden); CAS and CNSF (China); and the Alexander von Humboldt Foundation (Germany).

[1] S. Abachi *et al.* (D0 Collaboration), Phys. Rev. Lett. **74**, 2632 (1995).
[2] F. Abe *et al.* (CDF Collaboration), Phys. Rev. Lett. **74**, 2626 (1995).
[3] W. Marciano, arXiv:hep-ph/0411179.
[4] C. Amsler *et al.*, Phys. Lett. B **667**, 1 (2008).
[5] Tevatron Electroweak Working Group, Report No. FERMILAB-TM-2427-E, 2009.
[6] C. Hill, Phys. Lett. B **345**, 483 (1995).
[7] K. Lane and E. Eichten, Phys. Lett. B **352**, 382 (1995); **433**, 96 (1998).
[8] S. Dimopoulos and H. Georgi, Nucl. Phys. **B193**, 10 (1981).
[9] S. Heinemeyer *et al.*, J. High Energy Phys. 08 (2006) 052; S. Heinemeyer, W. Hollik, and G. Weiglein, Phys. Rep. **425**, 265 (2006); A. Djouadi *et al.*, Phys. Rev. Lett. **78**, 3626 (1997).
[10] B. Abbott *et al.* (D0 Collaboration), Phys. Rev. Lett. **82**, 4975 (1999).
[11] R. Dalitz and G. Goldstein, Phys. Rev. D **45**, 1531 (1992).
[12] K. Kondo, J. Phys. Soc. Jpn. **60**, 836 (1991); **57**, 4126 (1988).
[13] B. Abbott *et al.* (D0 Collaboration), Phys. Rev. Lett. **80**, 2063 (1998); Phys. Rev. D **60**, 052001 (1999).
[14] V. Abazov *et al.* (D0 Collaboration), Phys. Lett. B **655**, 7 (2007).
[15] A. Abulencia *et al.* (CDF Collaboration), Phys. Rev. D **73**, 112006 (2006).
[16] V. Abazov *et al.* (D0 Collaboration), Nucl. Instrum. Methods Phys. Res., Sect. A **565**, 463 (2006).
[17] G. Blazey *et al.*, in Proc. Workshop: QCD and Weak Boson Physics in Run II, edited by U. Bauer, R. Ellis, and D. Zappenfeld (FERMILAB Report No. FERMILAB-PUB-00-297, 2000).
[18] T. Scanlon, Ph.D. thesis, Imperial College, London [Report No. FERMILAB-THESIS-2006-43, 2006].
[19] V. Abazov *et al.* (D0 Collaboration), Phys. Rev. Lett. **101**, 062001 (2008).
[20] B. Abbott *et al.* (D0 Collaboration), Nucl. Instrum. Methods Phys. Res., Sect. A **424**, 352 (1999).
[21] V. Abazov *et al.* (D0 Collaboration), Phys. Rev. D **76**, 052006 (2007).
[22] T. Sjöstrand *et al.*, Comput. Phys. Commun. **135**, 238 (2001).
[23] M. Mangano *et al.*, J. High Energy Phys. 07 (2003) 001; M. Mangano, M. Moretti, and R. Pittau, Nucl. Phys. **B632**, 343 (2002); F. Caravaglios *et al.*, Nucl. Phys. **B539**, 215 (1999).
[24] D. J. Lange, Nucl. Instrum. and Methods Phys. Res., Sect. A **462**, 152 (2001).
[25] M. Mangano *et al.*, J. High Energy Phys. 01 (2007) 013.
[26] D. Stump *et al.*, J. High Energy Phys. 10 (2003) 046.
[27] R. Brun and F. Carminati, CERN Program Library Long Writeup W5013, 1993.
[28] V. M. Abazov *et al.* (D0 Collaboration), Phys. Lett. B **679**, 177 (2009).
[29] V. Abazov *et al.* (D0 Collaboration), Phys. Rev. Lett. **100**, 102002 (2008).
[30] R. Brun and F. Rademakers, Nucl. Instrum. Methods Phys. Res., Sect. A **389**, 81 (1997).
[31] F. James and M. Roos, Comput. Phys. Commun. **10**, 343 (1975).
[32] M. Bowler, Z. Phys. C **11**, 169 (1981).
[33] Y. Peters, K. Hamacher, and D. Wicke, Report No. FERMILAB-TM-2425-E, 2009.
[34] R. Field, Report No. FERMILAB-PUB-06-408-E, 2006.
[35] R. Field and R. Group, arXiv:hep-ph/0510198.
[36] R. Field, in CDF Run 2 Monte-Carlo Tunes, Proceedings of the TeV4LHC Workshop, Fermilab, October 21, 2005, (unpublished).
[37] V. Abazov *et al.* (D0 Collaboration), Phys. Rev. Lett. **101**, 182001 (2008).
[38] L. Lyons, D. Gibaut, and P. Clifford, Nucl. Instrum. Methods Phys. Res., Sect. A **270**, 110 (1988); A. Valassi, Nucl. Instrum. Methods Phys. Res., Sect. A **500**, 391 (2003).
[39] Tevatron Electroweak Working Group, Report No. FERMILAB-TM-2413-E, 2009.